Restoring cyclostationarity of rolling element bearing signals from the instantaneous phase of their envelope

Adrien Marsick, Hugo André, Ilyes Khelf, Quentin Leclère, Jérôme Antoni

Restoring cyclostationarity of rolling element bearing signals from the instantaneous phase of their envelope

Adrien Marsick[a,c,*], Hugo Andre[b], Ilyes Khelf[c], Quentin Leclère[a], Jerome Antoni[a]

[a] *Univ Lyon, INSA Lyon, LVA, EA677, 69621 Villeurbanne, France*
[b] *Univ Lyon, UJM Saint Etienne, LASPI, EA 3059, F-42334, IUT de Roanne, France*
[c] *Engie Green, 6 Rue Alexander Fleming, 69007 Lyon, France*

Abstract

Rolling element bearing signals are known to exhibit pseudo-cyclostationary properties that limit the efficiency of health monitoring. This paper investigates the restoration of cyclostationarity of train of impulses generated by bearing faults with the definition of a bearing angle-time relationship. Two main contributions structure the present paper. The first part presents a unifying synthesis of the state of art on the issue. The concept of *cycle of reference* (CoR) for cyclostationarity is presented. The possible causes of the well-used concept of *slippage* of the rolling-element bearing are explored to highlight the limitations of the cyclostationary theoretical framework. The influence of different types of jitters is presented to show the effect of using shaft cycle of reference on the spectral properties. CoR, on which bearing signals are phase locked so to restore their cyclostationarity, and a method to estimate the appropriate angle-time relationship are introduced. In a second part, original contributions on demodulation parameters and the possible introduction of unwanted artefacts are thoroughly explained along with the definition of a hypothesis test. The superiority of cyclostationarity restoration for monitoring purposes is illustrated on two industrial cases.

Keywords: condition monitoring, rolling bearing, slippage, skidding, order tracking, cyclostationarity, pseudo-cyclostationarity

1. Introduction

Monitoring the actual condition of a system is highly valuable to ensure its safety and extend its service life. Rolling bearings are fragile key components in rotating machinery. There is a need to detect, diagnose and assess the remaining useful life of rolling bearings. In the past decades, numerous methods have been developed to monitor industrial machinery using thermography [1], lubricant analysis [2], electric signature [3], acoustic emission [4], or instantaneous angular speed [5]. Still, vibration analysis is the widest method used in condition monitoring as it enjoys a wealth of dedicated signal processing techniques applied for decades in the industry. When monitoring industrial machinery, the vibration signals are most of the time a complex mixture of different components. The signal can be modelled as the sum of multiple sources distorted by the transmission paths of the structure, from emission to the measurement point. Unfortunately, the fault signature is often weak compared to other sources of noise in the signal. Modern condition monitoring relies on the separate study of the signal of interest without pollution from other sources based on its unique statistical properties. Indeed, most of the faults in rotating machinery translate into the generation of forces, synchronous with the rotation of a kinematic component. Faults signatures will exhibit periodic statistical properties, well described by the cyclostationary theory, on which most modern health monitoring signal processing tools are based. The cyclic properties of the fault signature are exploited for the design indicators in the spectral domain, for dedicated signal processing tools such as synchronous averaging and source separation [6]. Other tools rely on the amplitude distribution of fault signal with features like sparsity indexes [7–9]. The condition indicators based on these features are relatively insensitive to the issues addressed in this article but are less capable in terms

*Corresponding author
Email address: adrien.marsick@insa-lyon.fr (Adrien Marsick)

of fault localisation. Indeed, knowing the kinematics of the machine and the rotational speed allows pinpointing specific cyclic frequencies symptomatic of a defect. However, most of the signals are described as a function of time where the cyclostationary properties do not hold whenever the rotating speed is non-stationary. To handle this issue, scholars developed methods of order-tracking where the signal is numerically synchronised to the natural cycle of reference (CoR) where its cyclostationary properties are restored [10]. This resynchronisation operation uses an angle-time relationship and its tacholess estimation has been the focus of numerous methods in the past few years [11]. It showed to be effective in handling speed non-stationarity for gear-related signals and improved greatly the study of bearing faults. Yet, bearings are prone to experience phenomena that make the vibrations generated by the bearings lose their cyclostationary properties when seen from the revolution of the shafts. Commonly gathered behind the well-used concept of *slippage*, the loss of cyclostationarity can be caused by numerous reasons. This small amount of randomness at the impact instant, also called *jitter*, causes the bearing vibration to be described by what has been coined pseudo-cyclostationarity [12]. While showing little difference for diagnostic, it limits the application of signal processing tools previously described. Despite a few attempts [13, 14], the synchronous average of bearing faults is still limited, and the spectral peaks associated with the faults are known to spill over adjacent frequency bins.

The intuition on the possibility of using the appropriate CoR for bearing signals has been foreseen in a few precursory works. Mc Fadden and Toozhy [13] first described a synchronous averaging method using the relative speed between the races and the cage, using dedicated instrumentation to obtain the trigger signal. Siegel et al. [15] generated a tachometer signal from the envelope to estimate the phase of the impulses using Hilbert demodulation. The tachometer signal was then used to obtain a defect-synchronous average spectrum. One of the findings was that using the defect phase would permit better amplitude-based indicators in terms of sensitivity and consistency. Zhao et al. [16] presented a similar tacholess envelope technique to extract the phase of the impulses for resampling purposes, but without any reference to slippage. It comes to the work of Yan et al. [17], using the same method based on Hilbert demodulation, to explicit the link with bearing slippage without explicitly referring to pseudo-cyclostationarity. Yan et al. [18] proposed an improved shaft speed estimation aiming at a better evaluation of the skidding rate. Wang et al. [19] used a very similar scheme to use the phase of the impulses caused by the fault from the envelope signal. The extraction of the phase of the impulses was then improved in [20] using complex wavelet transform. Lu et al. [21] used a transient model based on wavelets to identify the impact instants and resample the signal to avoid smearing. Zhang et al. [22] used the phase of demodulated bearing fault in the envelope signal to resample equi-angle signals to average Wigner-Ville spectra for spall size estimation. All the presented works observe the limits of using the shaft's angle for resampling due to bearing slippage and highlight the benefits of finding the phase of the impulses. To do so, each of the works investigate various way to isolate the carriers of the phase of the impulses. However, while the underlying goal is to bring out the cyclostationary information of the train of impulses, no clear link to the cyclostationary theory has been made to the best of the authors' knowledge. Further, blindly using the instantaneous phase of the envelope to restore cyclostationarity of bearing signals may create artefacts in the signal causing false alarms. These artefacts were not described in previous works and no statistical method has been developed to limit their effect for the monitoring of mechanical systems.

In the light of the cyclostationary theory, the ambition of this paper is to fill these gaps to provide a theoretical base that will allow a better understanding of the capacities of such methods. To do so, the article is organised in two main parts. First, section 2 presents a unifying synthesis of the issue of pseudo cyclostationarity of rolling bearing signals. Section 2.1 introduces the concept of cycle of reference (CoR) for cyclostationarity and recalls the principles of angular approaches for gear-related signals. Then, the case of rolling bearing is thoroughly described with the derivation of fault frequencies with a perfect rolling assumption and its limitations. The concept of *slippage* is examined as a variation of characteristic frequency that can be caused by other factors than the slippage of rolling-elements. The limitations of classical amplitude-based health indicators with a growing fault are brought to light. At this point of the analysis, the influence of uncertainty on the instant of the impulses on the signal cyclic properties is presented within the framework of cyclostationarity. Section 2.2 provides a mathematical model of vibration generated by cyclic impulsive events that incorporates different models of jitter. The influence of such randomness is shown to have an impact on the spectral properties on which health monitoring indicators rely. Section 2.3 relates the cyclostationarity loss to new CoR for bearing events and links them with usual fault cyclic frequencies. These CoR substitute the traditional concept of slippage for the existence of two independent angular variables, from the bearing and the races rotations. A method aiming at estimating the new angle-time relationship is presented and illustrated with numerical examples.

Based on the models and the synthesis of the state of the art presented in Section 2, Section 3 introduces original contributions on the particularity of synchronisation for bearing related events. Namely, the importance of estimation errors for the new angle variable is addressed as well as the introduction of the pitfalls that are ahead of the automation of such methods to monitor a fleet of machines. Despite the clear advantages of the proposed method, it may introduce artefacts that can lead to erroneous interpretations. A thorough analysis of the causes for such phenomenon is proposed. Based on these theoretical developments, a robust method is introduced to limit the effect of artefacts. Finally, Section 3.2 offers a demonstration of the advantages of using the new CoR for substantial applications where bearings are prone to lose their cyclic properties. The method is applied to signals from a jet engine and the run-to-failure surveillance of a wind turbine gearbox.

2. A unified view of pseudo cyclostationarity for rolling element bearing signals

2.1. Cycle of reference (CoR) for rotating machinery

2.1.1. Cyclostationarity of machine signals and the use of angular resampling

A cyclostationary process is a stochastic process that carries periodicity in its statistical properties. As described by Antoni et al. [23], a process $\{x(\theta)\}_{\theta\in\mathbb{R}}$ is said to be strict-sense cyclostationary with cycle Θ if its joint probability function p_x is periodic in θ with period Θ

$$p_x(x_1, ..., x_m; \theta_1, ..., \theta_m) = p_x(x_1, ..., x_m; \theta_1 + \Theta, ..., \theta_m + \Theta), \tag{1}$$

where θ is a generic variable which is not necessarily time. A cyclostationary process is said to be of order n (CSn) if its n^{th}-order moment is periodic with period Θ. For instance, cyclostationarity at the first order (CS1) is defined by the expected value $m_x(\theta)$ being periodic with period Θ

$$m_x(\theta) = \mathrm{E}\{x(\theta)\} = m_x(\theta + \Theta). \tag{2}$$

Similarly, cyclostationarity at the second order (CS2) is defined by periodic second-order moments, especially its autocorrelation function

$$R_{2x}(\theta_1, \theta_2) = \mathrm{E}\{x^*(\theta_1)x(\theta_2)\} = R_{2x}(\theta_1 + \Theta, \theta_2 + \Theta). \tag{3}$$

Rotating machinery signals have been largely described with the framework of cyclostationary processes. The diagnostic methods based on these properties take advantage of the periodicity of statistical properties of signals. Most of the condition monitoring strategies rely usually on vibrations signals but can also encompass other types of signals generated by the operation of the machine such as strain signals or instantaneous angular speed. The raw signals are complex and include different sources of interest that distinguish from one another by their statistical properties. For example, imbalance, misalignment and gear meshing will produce CS1 signals with periodicity defined by the kinematics of the machine. On the other hand, CS2 signals, being periodic flows of energy, are likely to be generated by wear, friction forces, impacting forces, fluid motions or combustion forces. Faults in the machine are likely to be tied to a kinematic element and would exhibit cyclostationary properties that are used for detection, localisation and severity estimation. Diagnostic tools frequently rely on the cyclic properties of the fault signature. Health indicators are often based on the monitoring of a peak amplitude in a spectrum [24, 25] and synchronous average techniques have shown to be valuable for gears diagnostic [26]. Higher-order cyclostationary (CSn) is usually not exploited for condition monitoring as most rotating machinery signals are well described by CS1 and CS2.

In practice, most of the signals are not described with the appropriate observation variable where the signal exhibits its cyclostationarity properties. As an example for signals described as a function of time, rotating speed fluctuations of the machine during the observation windows cause the signal to lose its time-cyclostationarity. Yet, even when machines are subjected to large speed variations, the related events are synchronised with the rotation of a kinematic component. These signals are periodic with respect to this locking angle variable θ. If such signals are described with this generic angle of interest and not per time, they should take benefit from the angular periodicity of the events and regain the CSn properties of Eqs. (2,3) regardless of the speed variations. For any signal $x(\theta)$ described with respect to the angular variable θ, the spectral counterpart $X(\alpha)$ is simply the Fourier transform with respect to θ, namely

$$X(\alpha) = \int_{-\infty}^{+\infty} x(\theta)e^{-j\alpha\theta}d\theta, \tag{4}$$

where $j = \sqrt{-1}$, α the angle frequency and θ the observation variable, not necessarily time. The Fourier transform of Eq. (4) is not a function of frequency (inverse of time in Hz) but of an angle frequency α reflecting events per revolution of the CoR. The CoR is linked to the angular position of rotating parts like gears or bearings [27].

The sampling strategy dictates the observation variable of a signal. Even if it is possible to sample the signal directly in the cycle of interest (e.g. using an optical encoder and dedicated data acquisition card), it is easier to acquire the signal in time and then resample it digitally with the help of a *generic variable*-time relationship $\theta(t)$. This method known as *order-tracking* permits synchronising signals with respect to new angular variables. The angle-time relationship is of great interest in the case of vibration signals where cyclic impacts excite resonances of the system. Indeed, faults signature are well described with a class of angle-time cyclo-stationary signals where a cyclic train of impacts excites time-dependent resonances of the structure, as described by Abboud et al. [28, 29].

A wealth of tacholess techniques has been developed to extract the angle-time relationships from the signal itself and are thoroughly described by Peeters et. al in [11]. However, it started by the breakthrough work done by Bonnardot et. al [30] who first used the phase of the analytical band-passed signal around a meshing frequency of a geared transmission for resampling purposes. Order tracking for gears related signals has been widely used and proved to be effective to handle speed non-stationary operating conditions. Gears signals are better described with a generic variable of shaft angle better than a time variable since the forces applied to the system are synchronous with the shaft rotation. As such, the use of order tracking is known to avoid the smearing of the related frequency components in the spectrum. The vagueness caused by the related mechanical energy to be spread on different frequency bins is shown to be refocused around a unique frequency bin after order tracking despite the inevitable transmission error. At first orders, kinematics impose proportionality between the instantaneous frequency of meshing and that of the shaft. From this rotational instantaneous frequency, the instantaneous phase $\theta(t)$ can be recovered by their integral relationship.

To conclude, the key idea is that with the adequate *generic variable*-time relationship, one can restore to some degree the cyclostationary properties of rotating machinery signals previously described in time. This method proved to be highly effective for gear signals and improved the diagnosis of bearings.

2.1.2. Slip in rolling-element bearing and impact on classical diagnosis

The resynchronisation of gear-related signals to a reference shaft rotation is an efficient method to restore their cyclostationarity since the generated force are synchronous with the rotation and can be used to monitor complex gear systems. Concerning bearing signals, their CoR are closely related to a reference shaft. Yet, the forces acting on the system are not exactly synchronous with the shaft. Due to the small desynchronisation from the shafts, such signals were coined pseudo-cyclostationary [31] and this property limits the monitoring applications. The origins of such deviations to cyclostationarity properties will be developed in what follows. The goal is not to give an extended dynamic model of rolling bearing operation but rather general rules of thumb to apprehend the properties of such signals.

Kinematics of rolling-element bearing with perfect rolling assumptions.

Rolling-element bearing (REB) are basic components for mechanical transmission where the main load is transferred through elements in rolling contact rather than sliding contact [32]. Classical bearings are described by a few geometric quantities summed up in Fig.1, presenting a schematic of a classic angular contact bearing. The fundamental components of REB are the outer race, the inner race, the cage and the rolling elements (RE). The defining features are the number of rolling elements Z, the element diameter d, the pitch diameter D and the load contact angle β. In what follows, subscripts I,O,C will respectively refer to the inner race, outer race and the cage. Considering that the contact angle is the same for each rolling element, the races diameter can be expressed from the pitch diameter D, that is $D_I = D - d\cos(\beta)$ and $D_O = D + d\cos(\beta)$. Each race has an orbital angular velocity with respect to a fixed origin, located at the centre of the bearing f_{*/R_0}. For the sake of readability, the rotation reference is assumed to be the fixed origin whenever it is absent. The displacement of the k^{th} rolling element is defined by its spin angular velocity $f_{R,k}$ with respect to its own centre. The cage distributes the rolling elements among the pitch circumference. In a model where the displacements of the rolling elements are considered small with respect to the cage, the train fundamental circumferential and angular velocities are referring to displacements of the centre of rolling elements, identical to that of the cage. That is the circumferential speed V_k is the same for every rolling element and the cage, forming an equivalent rigid body, the *fundamental train*. With this assumption of perfect rolling (PR), the fundamental train

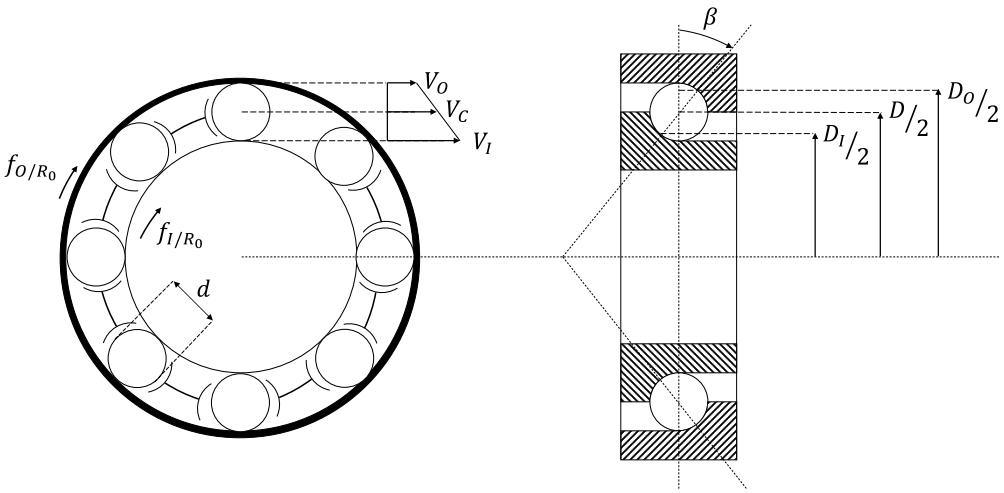

Figure 1: Schematic rolling element bearing components

linear circumferential velocity V_C is the mean value of that of the inner and outer races V_I and V_O, that is

$$V_C = \frac{V_I + V_O}{2}. \tag{5}$$

When operating, the interaction of a rolling surface with incipient faults caused by a local loss of material in one of the bearing elements will produce a train of impulses with cyclic frequency depending on the geometric properties of the REB and the rotation speed of the races. As described by Howard [33], the classical equations for bearing fault frequencies are easily derived and summed up in Table 1.

Table 1: Cyclic events occurring in rolling bearing operation.

Event	Acronym	Angle frequency
Ball Pass Frequency Outer Race	BPFO	$\frac{Z}{2}(f_I - f_O)\left[1 - d/D\cos(\beta)\right]$
Ball Pass Frequency Inner Race	BPFI	$\frac{Z}{2}(f_I - f_O)\left[1 + d/D\cos(\beta)\right]$
Fundamental Train Frequency	FTF	$\frac{f_I\left[1-d/D\cos(\beta)\right]}{2} + \frac{f_O\left[1+d/D\cos(\beta)\right]}{2}$
Ball Spin frequency	BSF	$\frac{D}{2d}(f_I - f_O)\left[1 - (d/D\cos(\beta))^2\right]$

Experimental observations refuting perfect rolling.

In practice, two experimental observations contradict the hypothesis of perfect rolling. As shown schematically in Fig. 2, peaks in the spectrum differ from the theory as being shifted in the neighbourhood of the fault frequency and spread out in multiple frequency bins compared to the expected pure rolling hypothesis. The framework of perfect rolling is purely theoretical, and the differences observed with experimental applications have been reported for a long time. Taylor [34] soon proposed that the deviation could be caused by wrong contact angle estimation and slippage. The effect of uncertainties of internal geometry of REB was studied by Springer [35], but yet, the significant offset from the theoretical frequencies observed cannot be explained only by a misidentified contact line. With the assumption of a known contact angle, this shift is caused by the train linear circumferential velocity to differ from the mean value proposed in Eq. (5). This deviation was found to be sensitive to loading conditions, lubrication and variable speed profile [36]. Pennacchi et al. [37] showed experimentally that this deviation was biased toward the direction where the cage rotational speed is lower than expected for a fixed outer race.

Second, the fault signature is unlikely to be perfectly cyclic. The train of impulses is slightly asynchronous with a strong influence on the signal properties. The radial-to-axial load ratio may change during the observation window and impact the contact angle. Additionally, even with a hypothetical fixed load ratio, randomness at the time of arrival

of the impulses also causes the fault signature to lose its cyclicity. While ideally yielding a narrow peak in the spectral domain, the quasi-periodicity of the fault signature causes the peak distribution to broaden.

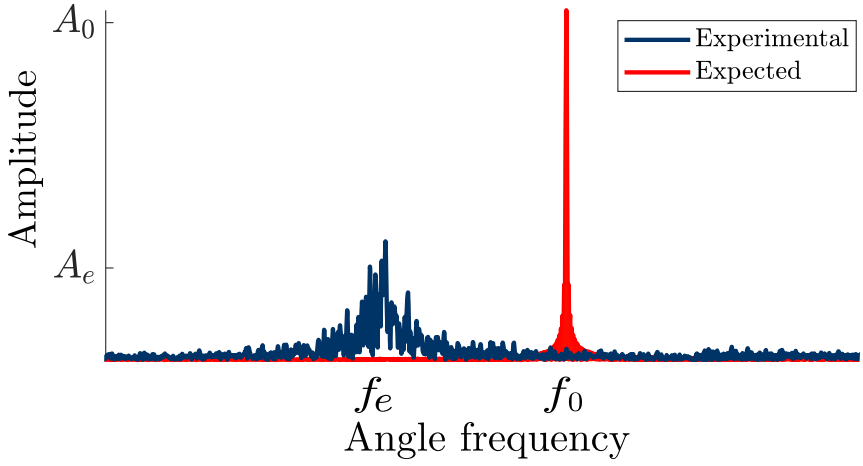

Figure 2: Schematic of difference between expected spectral peaks with perfect rolling theory and experimental observations. The expected frequency using the perfect rolling assumption is f_0 and the mean frequency of the observed experimental peak is f_e.

Kinematic models with slippage.

The deviation from perfect rolling expectations originates from the interaction between the rolling elements, cage and races with a direct impact on the signal properties. Unlike gears whose kinematic elements cannot slip, the rotation of the rolling elements and the cage are the fruit of complex interactions. As such, the impulsive forces generated by the bearing faults are not exactly locked to the rotation of a shaft of reference (inner or outer race) but experience small variations around it, depending on the operating conditions. Numerous methods with increasing complexity [38–42] have been developed to model accurate representations of slippage. In these models, a relative motion between the rolling elements and the cage is allowed. Each rolling element is subject to contact forces from races and the cage. The magnitude and direction of these contact forces vary during a revolution with a direct effect on the speed of the rolling elements. Each rolling element has a different effective rolling diameter. This effective diameter depends on the axial-radial load ratio causing the races and RE to bend away from circularity. As a direct effect, each RE runs faster or slower during one revolution than the cage. Despite the speed differences, the cage forces the rolling elements to maintain a similar speed, forcing slippage between rolling elements and both races. During a revolution, the rolling elements tend to drive the cage in the loaded region and to be driven by the cage in the unloaded region, as described by Liu et al. [42]. Since the cage itself is set in motion by the interaction with the loaded RE, there is no reason why the pushing and pulling would compensate to make the mean speed equal to the relationship of Eq. (5). A local loss of speed from a rolling element will impact the cage speed that will eventually pass to the overall set of rolling elements.

Another source of speed variation of individual rolling elements is the presence of a local fault. Local interaction between the RE and the spall will at the same time induce mechanical energy dissipation and introduce randomness. Models [43–46] describe the interaction as successive events. At the entry, the RE is partially or totally unloaded, redistributing the load to other elements. Then, the RE impacts the races while progressively recovering its nominal load. The spall geometry described in the references uses simplified square faults, but complex spall geometry will only accentuate the phenomenon with multiple impulsive events while reloading. For complex spall geometries, these impulses create a periodic flow of mechanical energy with non-reproducible waveforms with CS2 properties. The goal here is not to describe the models in depth but to highlight the fact that the interaction with a spall is not trivial. The abrupt unloading and the forthcoming impact will certainly affect the local RE circumferential speed and thus increase the deviation from the hypothesis of perfect rolling.

The loss of linear dependence with the races rotations introduces two differences: first, the mean slippage will change the average duration of the cycle thus giving the frequency shift shown in Fig. 2. At the same time, the

non-reproducible interactions between the RE, races and cage will change the distribution of inter-arrival of impacts that will destroy the periodicity when seen from the races' rotations. The extension and the intensity of slippage depend on the angular acceleration of the races, the loading and lubrication [42, 47]. Unfortunately, varying load and speed operating conditions at a short-time scale are inevitable in condition monitoring of machinery such as the ones encountered in wind turbine monitoring context. Monitoring strategies in such fields are likely to suffer more from these features than machines operating in stationary conditions. Focusing on the inter-arrival time distribution, simple models of randomness have been developed by Randall and Antoni in [31] to describe the complex phenomenological slippage phenomenon. The loss of cyclicity motivated the designation of *pseudo-cyclostationarity* to describe such signals. The intuition motivating the present paper is that with a growing fault, both the loss of mechanical energy during the revolution of the cage and randomness increase, changing the average cycle as well as the probability distribution of the inter-arrival time of impact. As the defect extends, monitoring indicators based on a spectral amplitude could be weakened by pseudo-CSn properties.

To sum up, the loss of cyclicity virtually always occurs in rolling bearing operation. During the acquisition period, the fault characteristic frequency is likely to vary due to various causes such as a change in the equivalent contact angle or non reproducible interactions due to the slippage of rolling elements. The traditional concept of *slippage*, which encompasses all these contributions, expresses the loss of a simple relationship between the cage and the races rotations. Far from the idealised model of the fundamental train, individual rolling elements run at their own circumferential speed depending on operating conditions and weaken the perfect rolling hypothesis. These phenomena are likely to be intensified with load and speed non-stationary conditions. From a monitoring point of view, the distribution smearing in the frequency domain has a strong impact on amplitude-based health indicators. For low signal-to-noise ratios, the loss of cyclicity makes the fault difficult to detect. In addition, the amplitude of a spread peak is difficult to define and does not necessarily reflect the mechanical energy released by the fault. While it has been said that the deviation from PR introduces both a frequency offset and pseudo-cyclostationarity properties, the work will focus on the latter aspect.

2.2. Modelling of impact instants and vibration processes

2.2.1. From impact to vibration, a generic model

It seems important to discuss the underlying impact process, the effect of randomness and the consequences on the spectral quantities with simple models. Most of the fault signatures are described by a train of impulses occurring whenever a spall interacts with a mating surface. As described by Antoni and Randall in [48], the impacting process $F(t)$ describes the succession of impacts instants T_i where the reference time $T_0 = 0$ is chosen to coincide with the first impact. That is,

$$F(t) = \sum_{i=0}^{\infty} \delta(t - T_i), \tag{6}$$

where the use of the Dirac comb is a valid idealisation of the impact process if the excitation band is large with respect to the bandwidth of the measure. In what follows, let $\{T_i\}$ be the stochastic process governing the arrival of the i*th* impact. The impact process is further described by the product densities of degrees one $f_1(t)$ and two $f_2(t, \tau)$ which can be interpreted respectively as the mean rate of an impact at the time t and the probability of an impact at time t and time $t + \tau$. The Fourier transforms of these products along t and τ are the specific spectral signatures $F_1(\alpha)$ and $F_2(\alpha, \omega)$. For impact processes with expected inter-arrival time instants $E\{T_i - T_{i-1}\} = T$, the spectral signature features repeating patterns of periodicity of $\alpha_0 = 1/T$.

Classical models [12, 49, 50] describing the transformation of the faulty bearing impact process $F(t)$ into a vibration $x(t)$ involve a modulating function $A(t)$ and the generally time-varying structural response of the system $g(t, \tau)$ at time t subjected to an impact at time τ, as shown in Fig. 3. Without loss of generality, $g(t, \tau)$ can also incorporate the cascade of filtering operations including the effect of the structure and additional user-defined band-pass filter. The additional filtering operation is usually done around a structural resonance of the system to enhance the signal-to-noise ratio (SNR). The mathematical model associated with such system is given by

$$x(t) = g(t, \tau) * [A(t)F(t)], \tag{7}$$

where the modulating function $A(t)$ represents the impact strength and incorporates random periodic modulations that could be caused by non-repeatable microscopic impacting process or the passage of the defect into the load zone.

Similarly, the structural response $g(t, \tau)$ can present similar periodicity with respect to the time variable t due to a

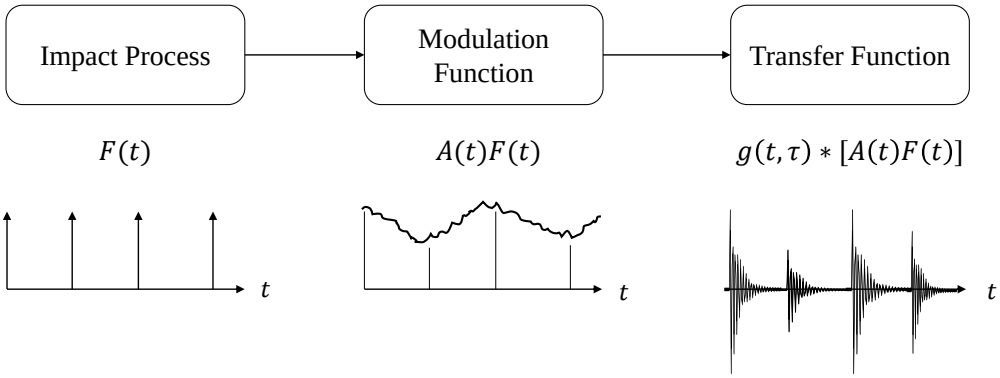

Figure 3: Model from impact process to vibration signal.

changing transfer path as the defect location moves with respect to the sensor. With these hypotheses, the modulating function $A(t)$ is assumed to be a second-order cyclostationary process with period Ω where the cycle is either related to the rotation of inner, outer race or the cage speed depending on the location of the fault. As shown in [48], the spectral quantities obtained from the vibration signal all heavily depend on the Fourier transforms of product densities of degrees one and two. The Fourier transform of the expected value of the vibration signal is the summation of filtering operations multiplied by the convolution of the Fourier transform of the product density of degree one $F_1(\alpha)$ of the impact process, with the modulation. The key point to remember is that $g(t, \tau)$ is likely to act as a band-pass filter in a high-frequency range for mechanical applications whereas the specific signature $F_1(\alpha)$ is quickly ruined for high frequencies as soon as randomness is introduced. To overcome these non-overlapping frequency ranges, the spectral correlation density of the vibration was shown to be the optimal candidate by Antoni [12]. Namely, the spectral correlation density of the band-pass signal S_X is the double Fourier transform along t and τ of the auto-correlation function R_{2x}. Like the spectral representation of the expected value, the spectral correlation function boils down to the product of the spectral signature $F_2(\alpha, \omega)$ modulated by the expected value of the modulation and weighted by the frequency response of $g(t, \tau)$. However, this time, the filtering effect of the structure specifically bandpasses the signal where the diagnostic information is available. This bi-variate representation preserves the diagnostic information but can be difficult to compute and interpret compared to a vectorial classical spectrum. It has been shown in [49] that the integrated spectral correlation in the ω direction is equivalent to the spectrum of the expected squared analytical band-passed signal and preserves its diagnostic information. The envelope spectrum is widely used in the industry due to its simplicity and lighter computational cost. It will be preferred in the applications that follow.

2.2.2. Models of impulse arrival time and the consequences on the signal characteristics

From the derivation of the previous vibration model, the key concept to understand here is that the spectral quantities on which modern condition monitoring indicators rely are all heavily dependent on the spectral $F_1(\alpha)$ and $F_2(\alpha, \omega)$ of the impact process. As such, identification, localisation and prognostic capacities are all dependent on the nature of the process driving $\{T_i\}$. In its simplest form, the impact process is totally deterministic such as $T_i = iT$, where T is the inter-arrival time of impacts. The product densities of degrees one and two are Dirac combs. The information is totally preserved in both the Fourier transform of the expected signal and the spectral correlation. Stochastic models of event arrival time will be described with two main models where the uncertainty on the event time is described by a cumulative or non-cumulative jitter [51]. The application to faulty bearing vibration signals has been presented in [12]. A recent generalised model derived by Borghesani et al. [52] did study the interaction of mixed jitters and proposed a way to measure them from a spectral approach. In this work, the effects of the two different types of jitter will be studied separately to highlight their differentiated effects.

Model of non-cumulative jitter (NCJ).

In the first model of randomness (coined *non-cumulative jitter*), the uncertainties on the arrival of the impacts are

independent of the previous or future occurrences such as

$$T_i = iT + \delta T_i, \tag{8}$$

where δT_i is an independent and identically distributed random variable of probability density function $\phi_\delta(T_i)$. Assuming a zero-mean density function, the random jitter will make the ith impact fall around the expected value of the node iT. For this model, the jitters δT_i are uncorrelated to the arrival times. The product densities can be described by the convolution of a Dirac comb Ш_T representing the nodes of the perfectly deterministic model, convoluted with a unique probability density function $\phi_\delta(t)$. Approximating the probability density function by a Gaussian distribution with zero-mean and standard deviation σ_Δ, the spectrum of density function of first order is a Dirac comb low-pass filtered by the characteristic function

$$\Phi_\delta(\alpha) \sim \exp\left(-\frac{1}{2}\sigma_\Delta^2\alpha^2\right), \tag{9}$$

where it becomes clear that peak amplitude tends towards zero for higher frequencies and is attenuated with a cut-off frequency of $\alpha_c \sim \sqrt{2}/\sigma_\Delta$. As described previously, the band-pass effect of the $g(t,\tau)$ will mask the signature due to different frequency support of filters. However, the distribution being the same for each impact, the auto-correlation function preserves the diagnostic information. The presented model introduces randomness but is representative of the assumption that the fundamental train speed is running at a fixed proportion from the races so that the randomness on the impact time only comes from the rolling element spacing within the cage. The fundamental train frequency is still assumed to be kinetically constrained to follow the mean speed of inner and outer races, that is the slip of rolling elements within the cage does not affect the overall cage rotational speed. This model is perfectly cyclostationary at the second-order hence the excellent diagnostic capacities of spectral correlation or envelope spectrum.

Model of cumulative jitter (CJ).

In practice, there is no reason why the cage would not deviate from Eq. (5), implying that the overall slippage of RE would compensate. A more accurate model of cumulative jitter (CJ) allows the cage to move away from the fundamental train model [50]. Herein, the inter-impact event interval $\Delta T_i = T_i - T_{i-1}$ is a random variable. The cumulative effect of the random walk can be written as

$$T_i = T_0 + \sum_{l=0}^{i} \Delta_{T_l}, \tag{10}$$

where Δ_{T_i} has a mean of T and standard deviation of σ_Δ. With this model, the probability density function for the ith impact $\phi_i(t)$ to occur $]t; t+\delta t]$ is different for each occurrence and the uncertainty of impact location increases with time. Based on Eq. (10), the probability density distribution of the ith peak $\phi_i(t)$ is the probability of the sum of independent variables which is the convolution of their probability density functions. The central limit theorem states that the actual distribution of the ith impact will be normally distributed with mean iT and standard deviation $\sqrt{i}\sigma$ given that each original distribution has a mean of T and deviation σ. The spectral signature of $F_1(\alpha)$ is still a succession of finite-energy periodic peaks with cycle $1/T$ but now the energy of the successive harmonics is gradually spreading out on increasing bandwidth with a quality factor of $Q_i \sim T^2/(i\pi\sigma_\Delta)^2$ [48].

The density functions of degree one and their spectral counterpart of the three models are summed up in Figs. (4-5), where the $\sigma_\Delta/T = 0.1$. For both stochastic models, the diagnostic information will be unavailable in high frequency ranges. The spectral signature is ruined for the model of non-cumulative jitter because of the low-pass effect, but the distribution of the peaks stays identically narrow. On the other hand, cumulative jitter yields a continuous spectrum with the cyclic energy being increasingly spread out. The additional consequence for cumulative jitter is the loss of second order cyclostationarity since $f_2(t,\tau)$ progressively reaches a constant value without any periodicity. For a small amount of random variations, the loss of cyclostationarity has a limited effect on diagnostic since the spectral signature is relatively preserved for the first faults harmonics. However, in this case, the energy is dispersed according to the jitter, which itself depends on the operating conditions or the presence of a fault. The amplitude of the peak is not representative of the intensity of the cyclic event. This point highlights the limitations of classical spectral monitoring to evaluate the gravity of the fault when it comes to rolling bearing.

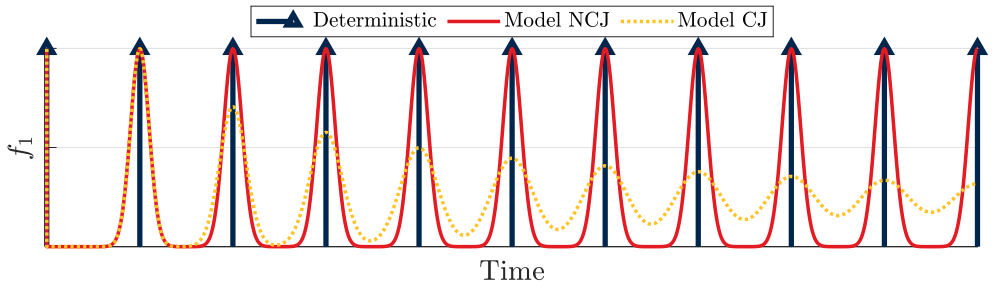

Figure 4: Density functions of the first order.

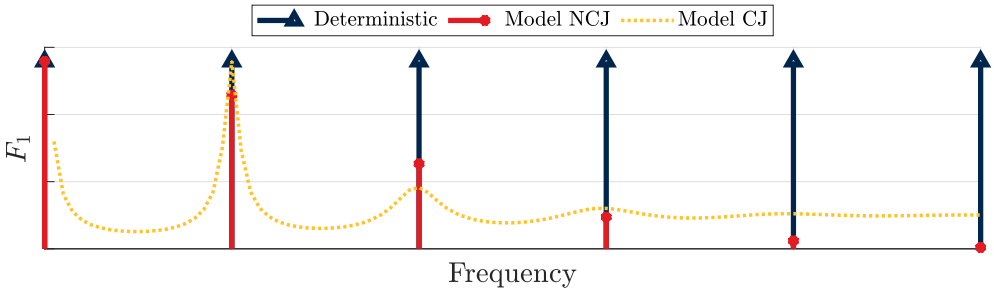

Figure 5: Spectrum of density functions of the first order.

2.3. Methodology for cyclostationarity restoration of rolling element bearing signals

The proposed method aiming at restoring the cyclostationarity of rolling-element bearing signals is summarised in Fig. 6. Using the CoR defined in section 2.3.1 and the estimation method of section 2.3.2, the vibration signal is synchronised in the CoR so to restore its CS properties.

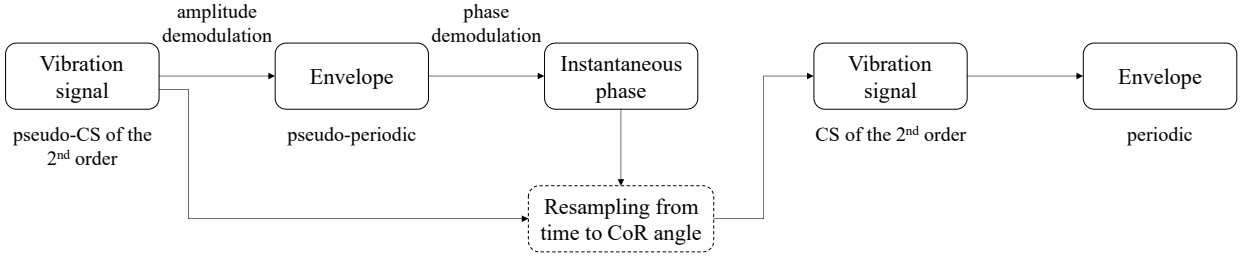

Figure 6: Flowchart for cyclostationarity restoration.

2.3.1. Cycles of reference for bearing related faults

In practice, treating pseudo-cyclostationary signals as cyclostationary shows little difference for detection, since the train of impulses will eventually carry enough mechanical energy for the peaks to emerge in the spectrum. Still, being *pseudo* narrows the palette of signal processing tools available for condition monitoring. The cycle randomness makes it impossible to define a cycle on which we could apply synchronous strategies nor accurately track the fault severity due to the energy spreading. However, similar to the existing proportionality relationship for gear meshing, CoR synchronous with bearing related events can be defined. Without restrictive assumptions on the perfect rolling hypothesis, the equations of Tab. 1 generalises to Tab. 2 as described by McFadden [13, 24]. The second line recalls the case of a meshing frequency for a gear. Here, the fault instantaneous frequency has been defined with the relative rotational speed. They are not defined with the fixed referential but between the elements of the bearing $f_{*/*}(t)$. For

instance, let the relative rotational speed between the outer race and the cage be defined as $f_{C/O}(t) = f_{C/R_0}(t) - f_{O/R_0}(t)$. Other relative rotation speeds can be constructed in the same way and the same applies for the relative spin between rolling elements and the cage $f_{R_k/C}(t)$.

Here, the *slippage* is totally enclosed within the relative speed. Identically to the fact that the shaft rotation comprises exactly the number of teeth events, the cycle of relative angular position between the cage and the races will comprise exactly Z passing rolling elements. Even if the representation of the fundamental train as a rigid body is invalidated with slippage, the frequencies relative to the cage $f_{C/*}$ are to be understand as the equivalent average rotation, shared by all the RE. The intrinsic cycles that restore the CSn properties are defined by these new rotational speeds of Table 2.

Table 2: Cyclic events of rotating machinery and their observation cycle.

Event	Cyclic frequency	Cycle of reference	Event per CoR
Meshing	Nf_{S/R_0}	f^{-1}_{S/R_0}	N
BPFO	$Zf_{C/O}$	$f^{-1}_{C/O}$	Z
BPFI	$Zf_{C/I}$	$f^{-1}_{C/I}$	Z
FTF	f_{C/R_0}	f^{-1}_{C/R_0}	1
BSF	$f_{R_k/C}$	$f^{-1}_{R_k/C}$	1

Theoretically, if one knows the relative speed of interest, the adequate *angle-time* relationship can be estimated. Then, the signal can be described with this new angular variable to provide insensitivity to the random walk of the jitter. It can be noted that even with a perfect resynchronisation, it will not change the intrinsic nature of the phenomenon at stake. Bearing faults are better described by CS2 events since the RE/spall interaction incorporates complex phase effects and non-reproducible interactions. However, one can hope that the CS1 part that was previously incorporated in the CS2 should be restored after resynchronisation if it exists.

2.3.2. Estimation of the CoR angle-time relationship from the phase of the impulses

The key challenge is thus to extract the instantaneous relative speed for appropriate synchronisation. It seems unfeasible for both practical and economic reasons to install an optical encoder to obtain the relative speed of the cage. Attempts have been made to measure the rotational speed of the cage [53], but a sole device would not be able to monitor complex systems as for shaft mounted encoders due to slippage. Fortunately, the same tacholess techniques developed for classical shaft order tracking can be exploited. Nevertheless, two challenges come out compared to classical shaft instantaneous phase estimation. Firstly, the impulse signal is better described as cyclostationary of second order. Therefore, the information about the train of impulses is not easily found in the raw signal but rather accessible in the bandpass envelope of the signal, which will be preferred. Secondly, demodulation techniques are easier for shafts since the instantaneous frequency is varying relatively slowly given strong variations are improbable due to the inertia of rotating shafts. The optimal shaft frequency usually varies smoothly and as a matter of fact, low-pass filtering strategies were found to be effective for noise reduction estimation [54]. This point does not hold for bearing phase demodulation where the random walk is not smoothed by inertia effects. Consequently, the tacholess phase estimation needs to provide enough resolution. An interesting feature to be noted is that the phases of the fault's impulses and the shaft are closely related and differ in the random walk due to slippage. The shaft phase can be used as a first estimation of the phase of the impulses.

In the past years, scholars have been driven by these intuitions to create methods dedicated to bearing phase demodulation. Although each of the works presented in the introduction has its own originality, all of them offer to address the previously described challenges: processing the signal to bring out carriers of the impulses' phase and estimate its the subtle variations. While not mentioned clearly in previous works, the goal is to highlight the available pseudo-CS2 information in the signal to estimate the relative cycles of Table 2.

The analysis presented in this work will rely on the Hilbert demodulation from the resampled envelope signal, close to the method developed by Yan et al. [17]. Fig. 7 shows a simplified diagram of the method flowchart, where the hypothesis test will be discussed in section 3.1.2. Along with the description of the method, a simulated vibration signal from a faulty bearing is generated for illustration purposes. In this example, a virtual shaft is rotating at the angular velocity f_s experiencing a linear speed variation between 10 and 20 Hz during a 10s signal. The signal is

sampled at the rate of 10kHz. A virtual train of cumulative jittered impulses is created with the model of random walk of Eq. (10). The inter-impact angle, Δ_{T_i} follows a Gaussian law with a mean angle equal to 1/10 of shaft rotation and standard deviation of 5% of the mean. The expected cyclic frequency of the fault is $\alpha_0 = 10 f_s$. To model the structure, the impact process is filtered with an auto-regressive model of natural frequency 3500 Hz and pole radius of 0.9.

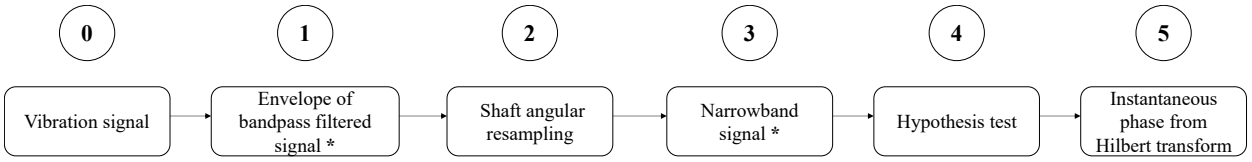

Figure 7: Flowchart for a robust estimation of the phase of the impulses. In the steps noted by the symbol $*$, key parameters influence the quality of the estimation.

In the first step, the signal is bandpassed in a frequency range where the signal-to-noise ratio is high. The frequency band where the impulses signature is enhanced is ideally corresponding to the resonances of the structure. Yan et al. [17], used the kurtogram developed by Antoni [55] to select the filter characteristics. Other approaches based on the selection of the appropriate filter in a filter-bank can be used [56–60] as long as frequency band carries the phase of the impulses. Then, the bandpass envelope is calculated with the help of Hilbert transform. At this step, the phase of the impulses is supposedly well defined in the envelope signal but incorporates both the speed variability of the shaft and the bearing slippage. Figure 8 presents the vibration signal for the first 0.05 s as well as its envelope, bandpass filtered between 3000 and 4000 Hz.

Figure 9 (a) presents the short-time Fourier transform of the envelope with original time sampling. The phase demodulation based on the analytical signal requires the isolation of the carrier from the rest of the spectrum by an ideal band-pass filter to comply with the mono-component assumption. However, with the shaft speed variability, the design of such a narrowband filter impact process may be complicated. To account for the variability of the shaft speed, the envelope is re-sampled with a synchronising signal from the shaft, giving the time-frequency representation of Fig. 9 (b). The shaft reference instantaneous phase signal is either provided from the signal of a tachometer or estimated from the signal itself with demodulation methods dedicated to shaft speed estimation. This processing step can be linked with iterative phase demodulation of [61]. The shaft resampling provides a first estimation of the phase, leaving only the slippage and estimation errors. With this newly resampled envelope signal, the impulses are well localised in a narrowband around the fault expected cyclic frequency.

At this point, the process is very similar to what has been done with shaft demodulation of supposedly speed stationary signals. The signal is filtered using a band-pass Butterworth filter in the order domain around the fault cyclic frequency α_0, here chosen with 4 epr width. The narrowband signal is ideally monocomponent and the phase is obtained by an unwrap operation on the phase of the analytic signal. Figure 10 compares the difference between demodulated phase obtained after the unwrapping procedure and the linear carrier component ($\alpha_0 t$) with the theoretical jitter saved during the signal generation. The process successfully estimated the phase of the impact showing a close match with the reference.

From this instantaneous phase, the appropriate CoR is extracted from the relationships of Table 2. Previous work [15] used the demodulated phase to focus on an equivalent *shaft phase* used as a tachometer for resampling purposes. However, this formalism eluded the definition of a CoR based on relative rotational speed of Table 2. While successfully handling slippage, the concept of equivalent shaft phase was hiding the true reference cycle in which the train of impulses was phase-locked so to restore its cyclostationarity properties. The new order domains presented in Table 2 are now relying only on relative rotating speed, allowing complex cases where both the inner and outer ring are rotating.

Then, appropriate order tracking procedure reassigns the same number of samples for each relative revolution of Table 2. Figure 11 presents the Fourier transform of the envelope order tracked with respect to the shaft cycle and the synchronised envelope, resampled with the newly demodulated phase. The angle frequency axis for resynchronised signal has been scaled to match with the original axis in event per revolution of shaft. Concerning the envelope signal synchronised with respect to the shaft phase, the random jitter causes the peak distribution at 10 epr to be spread out on

adjacent frequency bins. In agreement with the models of section 2.2, the flaring of higher harmonics peaks increases and the third harmonic does not emerge from background noise. In a model with added broadband noise, the impulses spectral signature will be ruined. However, after re-synchronisation with respect to the phase of the impulses, the spectral peaks are all narrowly distributed around the mean cyclic frequency of the impulses and its harmonics. The amplitude of successive harmonics is decreasing but at this point, no conclusion can be drawn whether the lowpass effect is caused by the bandpass filter of the envelope or a non-cumulative jitter effect described in section 2.2.

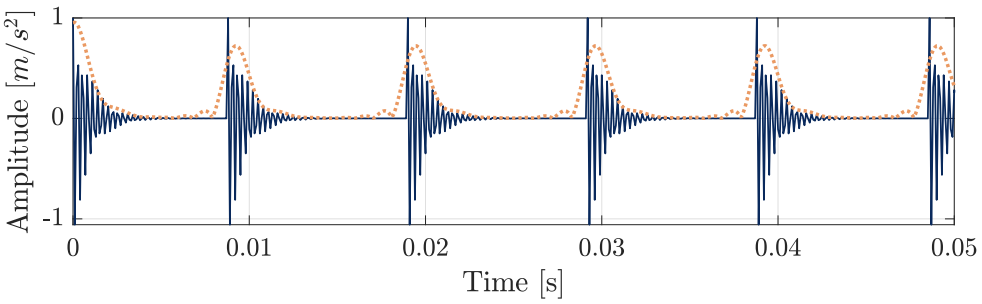

Figure 8: Extract of the simulated vibration signal (blue solid lines) and its envelope (orange dotted lines) filtered between 3000 and 4000 Hz.

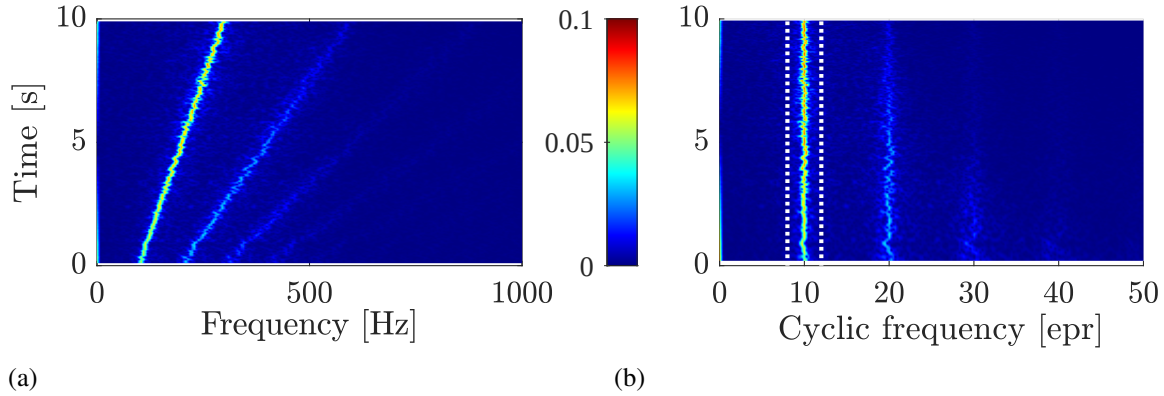

Figure 9: (a) Short-time Fourier transform of the envelope and (b) its synchronised version with respect to the shaft tachometer. The bandwidth of the narrowband filter is shown by the white vertical lines. The colour bar accounts for both and indicates the vibration amplitude in $[m/s^2]$.

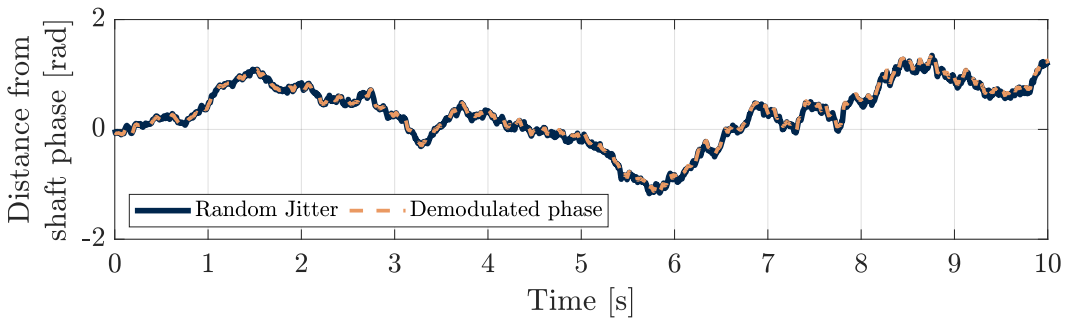

Figure 10: Comparison of phases from reference (blue lines) and demodulated phase (orange lines). The demodulated phase was estimated with a narrowband filter of bandwidth of 4 epr centred around α_0.

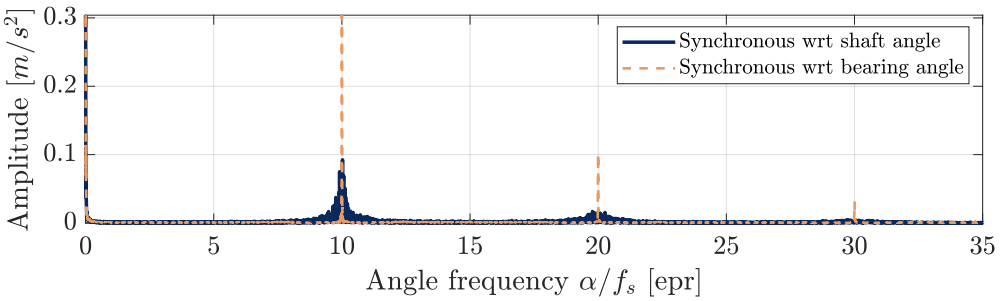

Figure 11: Spectrum of the envelope, synchronised with the shaft phase (blue) and with the phase of the impulses estimated by demodulation (orange), expressed in the order domain relative to f_s.

3. Original contributions

3.1. Toward an automated implementation, pitfalls and limitations of the method

3.1.1. The importance of bandwidth for narrowband filter

Compared to the phase of the shaft, the bearing demodulated phase incorporates higher frequency components. As pointed out before, this was not an issue for shaft-related speeds since the variations of their instantaneous frequency are relatively smooth due to inertia effects. In contrast for bearings, information about the phase jitter is available for every impact, or in other words, the jitter signal is sampled with a mean frequency equal to the cyclic frequency of the impulses $\alpha_0 = 2\pi/T$. Perfect reconstruction of the instantaneous phase for the sake of angular resampling would need to allow frequency content up to this angle frequency. However, the narrowband filtering operation on the analytical envelope of the signal low-passes the phase and smooths the variations caused by the random walk. The larger the bandwidth, the higher the frequency content of the demodulated phase. To illustrate this point, the effect of an ideal rectangular bandpass filter in the order domain of expression is studied in what follows. The transfer function of an ideal bandpass filter centered at α_0 and with a bandwidth Δ_α is,

$$H(\alpha) = \text{rect}\left(\frac{\alpha - \alpha_0}{\Delta_\alpha}\right). \tag{11}$$

On the other hand, the narrowband analytical signal x_F can be expressed as a combination of the instantaneous amplitude with a phase comprising the central frequency $\alpha_0 t$ and the residual $\phi_R(t)$.

$$x_F(t) = a(t)\mathrm{e}^{j\alpha_0 t + j\phi_R(t)} = x_R(t)\mathrm{e}^{j\alpha_0 t}, \tag{12}$$

where $x_R(t)$ can be recognised as the shifted version of the analytical signal in the frequency domain. The Fourier transform of Eq. (12) is

$$X(\alpha) = X_R(\alpha - \alpha_0), \tag{13}$$

where it is now clear that the band-pass filtering operation will act as a low-pass filter for the phase with bandwidth Δ_α. The maximal bandwidth to reconstruct the phase variations due to random walk is the target frequency, that is $\Delta_\alpha = \alpha_0$. Figure 12 presents a zoomed version of the residual phase of the signal $\phi_R(t)$ introduced in part 2.3.2. The blue line represents the reference phase saved during signal generation. Bandwidths of 2, 5 and 10 orders for the narrowband filter are tested to demodulate the phase, all centred around the cyclic frequency of the impacts $\alpha_0 = 10 f_s$.

The phases of Fig. 12 illustrate the low pass effect of the bandwidth. The demodulated phases are smoother for small bandwidths. With fractional bandwidth Δ_α/α_0 approaching unity, the frequency content of the phase is higher and display a better match with the actual variation of the phase caused by the random jitter. For cases where the demodulated phase is low passed, resampling the signal will correct the cumulative jitter with a smooth estimation of the instantaneous phase with limited frequency content. The actual impacts will occur at random positions around the new fixed nodes given by the demodulated phase, creating an artificial non-cumulative jitter.

The extracted phases are then used for synchronisation giving Figs. [13-14] showing respectively the Fourier transform of the signal and its envelope. The effect of such random error presented in part 2.2.2, is highlighted in Fig.

13. The Fourier transform of the signal is only the product in spectral domain of the Fourier transform transfer path coefficients and the distribution of that of the impact process $F_1(\alpha)$. For low fractional bandwidth, the low pass effect of the characteristic function $\Phi_I(\alpha)$ is caused by a higher deviation σ_Δ from the impact nodes. It can be noted that the distribution of the peaks is the same for every harmonic, meaning that the cumulative jitter has been corrected. For a unit fractional bandwidth, all the harmonics up to the Nyquist frequency are emerging, highlighting the fact that the demodulated phase is an accurate estimation of the jitter. The improvement of higher harmonics can be used as an indicator of the quality of the phase estimation. The amplitude of each peak reflects the effect of the convolution of the structure.

Figure 14 presents the spectrum of the envelope band-passed between 3 and 4 kHz. The envelope is either resampled with the shaft phase (blue lines) or with that of the impulses demodulated with different bandwidths Δ_α. As for the spectrum of the signal of Fig. 13, using the phase of the impulses for resampling sharpens the peaks. However, two phenomena low pass the envelope signal in this case. First, the previously presented effect of the jitter also applies here. Secondly, the bandpass filter, needed in the first step to obtain the envelope, takes the form of a low-pass filter in the envelope, which inevitably limits the occurrence of the peaks in the high frequency range. For both spectra, it can be noted that the amplitude of the first harmonics are sensibly the same, despite showing strong differences in higher frequency range. Indeed, when the peak to monitor is located at a low frequency significantly far from the cut-off frequency of the non-cumulative jitter low path filter, the difference between each estimation of the phase is low compared to the gain on the correction of cumulative jitter.

With these results, one would be tempted to choose a bandwidth for the narrowband filter equal to the cyclic frequency of the impulses. However, the numerical example does not incorporate any noise or additional cyclic components. In practice, it is almost impossible to have such large bandwidth, because other peaks in the envelope spectrum will jeopardise the monocomponent assumption and noise will contaminate the phase estimation. The issue of signal-to-interference ratio is a challenge for tacholess instantaneous speed estimation. Concerning the method of phase demodulation based on analytic signal, the recommendation is to use a well-separated harmonic with high signal-to-noise ratio [30]. Peeters et al. [11] gave an extensive review on tacholess speed estimation techniques with details on noise influence. Approaches on multi-harmonic demodulation [62], iterative phase demodulation [61] or the use of the Wigner-Ville distribution [63] tried to solve this issue. For now, the parameter selection of the envelope demodulation band, the suitable harmonic and the narrow demodulation bandwidth is made by trial and error, with certain room for improvement. Here, the message is rather about what methods with a low frequency estimation of the phase are capable to do and their limits. The random walk causing the peak distribution to be spread in the frequency domain is fixed without totally suppressing the randomness. The smoothed estimation of the phase transforms the errors of cumulative jitter into non-cumulative jitter. As a result, the cyclic peaks in the spectra are refocused but still experience a limited low-pass effect.

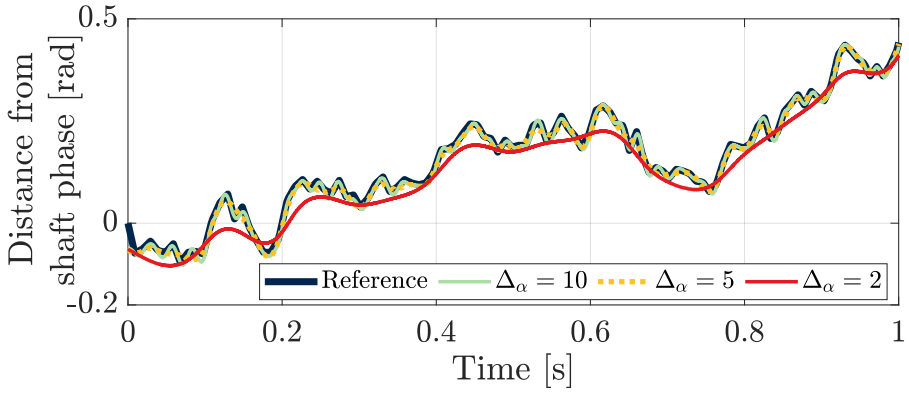

Figure 12: Comparison of phases from reference and demodulated phases estimated using different bandwidths Δ_α centred around α_0 indicated in legend. The reference phase is the same that as of the impulses of Fig. 10, with only one second shown.

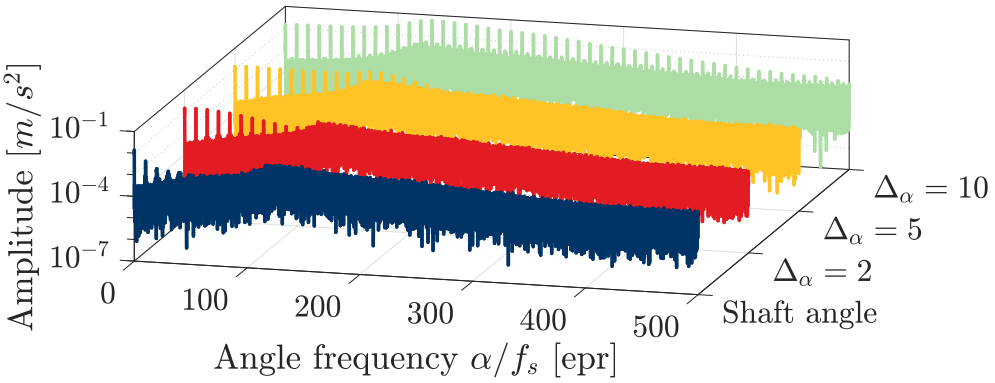

Figure 13: Spectrum of the signal, expressed in the order domain relative to f_s. The signal is either synchronised with respect to the phase of the shaft (blue lines) or to the demodulated phase estimated using different bandwidths Δ_α indicated in the Y-axis.

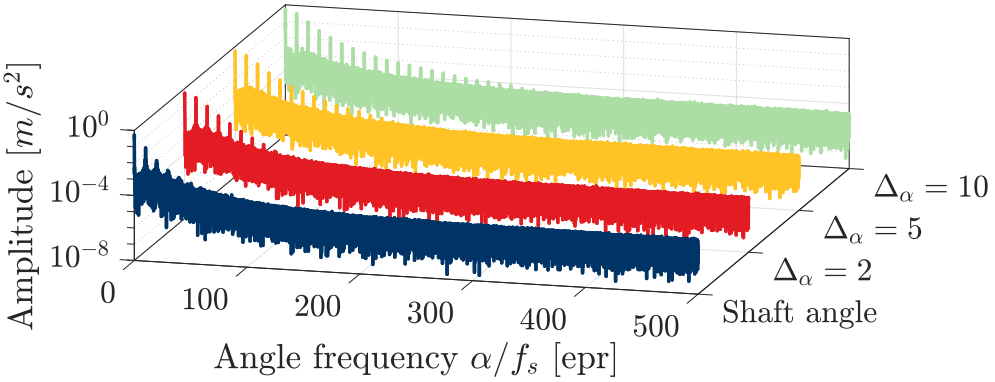

Figure 14: Spectrum of the envelope, expressed in the order domain relative to f_s. The envelope is either synchronised with respect to the phase of the shaft (blue lines) or to the demodulated phase estimated using different bandwidths Δ_α indicated in the Y-axis.

3.1.2. Artefact and mono component assumptions

Carrier peaks synchronous with the phase of interest are virtually always available for classical shaft phase demodulation since it is linked with the normal operating condition of the machine (e.g. meshing frequencies). A distinctive feature of the proposed application is that the demodulation medium for bearing, the *fault harmonics*, is present in the signal only when a fault appears.

Like all the tacholess instantaneous phase estimation techniques based on demodulation of analytical signal, the method described in part 2.3.2 relies on the assumption of a monocomponent signal. Yet, if one aims at automatic surveillance of industrial machinery, the demodulating band may contain only random noise. Figure 15 shows the envelope spectrum of a signal containing only a white Gaussian noise (blue) and the resampled envelope using the method previously described. The processing flow is exactly the one described in Fig.7 and applied in section 2.3.2, except for the input signal being a perfect white noise. Different bandwidths all centred on the presumed fault frequency are used for demodulation. The phase obtained from the narrowband signal are used for re-synchronisation. The spectra all exhibit a peak located on the mid-frequency of the bandpass signal used for demodulation, which may coincide with amplitude-based health indicators, potentially leading to erroneous diagnostic decisions.

The existence of a peak in an originally flat spectrum comes from the self-synchronisation of the signal. The narrowband signal $x_F(t)$ filtered around a midband cyclic frequency α_0 can be expressed as

$$x_F(t) = a(t)\mathrm{e}^{j\theta(t)}, \tag{14}$$

where $a(t)$ and $\theta(t)$ are respectively the instantaneous envelope and phase. As pointed out by Rice [64], the formalism

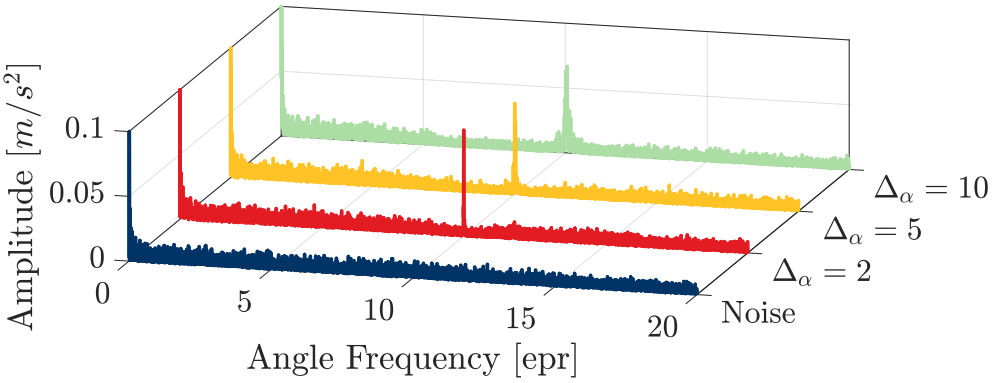

Figure 15: Spectrum of the envelope of a white noise signal expressed in the order domain relative to f_s. The envelope is either synchronised with respect to the phase of the virtual shaft (blue lines) or to the demodulated phase estimated using a narrowband filter centred around $\alpha_0 = 10 f_s$ with different bandwidths Δ_α indicated in the Y-axis.

of signal decomposition with instantaneous quantities is not restricted to narrowband signals but rather their interpretation as envelope and phase is limited for that case. That is, the instantaneous phase extracted from a bandpass signal containing noise would still exist but without any link to a jittered cyclic event. Unlike the phase extracted from meshing frequencies that always exist in the signal, the synchronising component in this case appears at the initiation of the fault. This feature compromises the automation of this method for early stages of the faults as the method creates cyclic artefacts in the signal. The originality of synchronising a signal from phase demodulation is that the angle $\theta(t)$ extracted from the narrowband feeds the synchronisation of the same signal so that Eq. (4) becomes

$$X(\alpha) = \int_{-\infty}^{+\infty} a(\theta(t)) \mathrm{e}^{-j(\alpha-1)\theta(t)} d\theta(t), \tag{15}$$

which can be recognised as the shifted Fourier transform of the instantaneous amplitude $a(t)$. When in presence of a cyclic component, the interpolation will narrow the peak previously spread on different frequency bins. Unfortunately, as shown in what follows, the spectral counterpart of a band-limited white noise resembles a relatively narrow peak, illustrated in Fig. 15.

As described by Rice [64], the envelope of a narrowband Gaussian process with added harmonic signal follows a Rice distribution whose probability density function is defined as

$$f(a|\nu,\sigma) = \frac{a}{\sigma^2} e^{-\frac{a^2+\nu^2}{2\sigma^2}} I_0\left(\frac{a\nu}{\sigma^2}\right), \tag{16}$$

where ν is the non-centrality parameter, σ the scale parameter, and I_0 the zeroth-order modified Bessel function of the first kind. When the harmonic signal is absent, the distribution simplifies to a Rayleigh distribution, a special case where the non-centrality parameter is null. In this case, Lawson and Uhlenbeck [65] have shown that the power spectral density of the envelope of a bandpassed white signal can be approximated by a triangular shape whose base is proportional to the bandwidth

$$A^2(\alpha)_{\Delta_\alpha,\rho} \approx \pi \Delta_\alpha \rho \delta(\alpha) + \frac{\pi\rho}{4\Delta_\alpha}(\Delta_\alpha - \alpha), \tag{17}$$

where ρ is the power spectral density of the noise and Δ_α the bandwidth of the filter. With Eq. (15), the spectral distribution of Eq. (17) will be shifted towards the new cyclic frequency of reference. In view of Eq. (17), the general rule of thumb would be that for large bandwidth the spectrum would become broader and flatter since the energy is dispersed. It matches well the increase of peak bandwidth inversely with the bandwidth of the narrowband signal displayed in Fig. 14.

From a practical point of view, there is a need to discriminate whether an observed peak is due to a cyclic event or self-synchronised noise. A first check in light of Eq. (15) is that a self-synchronised noise will only create a peak located in the vicinity of the midband frequency. If one observes other peaks enhancement in the spectrum, for

instance at higher harmonics or modulation sidebands, it can be assured that the demodulated phase actually comes from a cyclic event. However, testing the existence of a peak in the spectrum may be hard to quantify. The robustness of an amplitude-based statistical threshold on the presence of a peak, or the use of spectral sparsity measures in the original spectrum would depend on its emergence which was previously shown to be linked to the intensity of the jitter. Alternatively, one can test from the bandpass filtered envelope to assess the presence of a harmonic signal using its amplitude distribution. Statistical tests to assess the hypothesis of a Rician distribution against a Rayleigh have been developed by Giunta, Vandendorpe and Benedetto in [66, 67]. The hypothesis of the bandpass signal hiding a jittered harmonic component is accepted whether a testing variable is higher than a fixed threshold given a false-alarm probability. Appendix A presents the keys steps of the test from [66]. Using the envelope amplitude distribution takes advantage of its relative independence from the effects of jitters, as long as enough sampling points are chosen to cover the periodicity of the phenomenon at stake. The proposed approach will be tested on the run-to-failure industrial application of section 3.2.2.

3.2. Experimental validation based on industrial applications

This section intends to illustrate the previous concepts. The illustration relies on two experimental datasets with faulty bearings from a jet engine gearbox and a wind turbine. The first one is publicly available dataset and well-known by the condition monitoring community. The later dataset is a run-to-failure experiment coming from an industrial wind turbine. They proved to be good illustrators of the concepts developed earlier as they were prone to experience a higher loss of cyclostationarity caused by non-stationary conditions.

3.2.1. Surveillance 8 challenge: Vibration-based diagnosis of a Safran aircraft engine

The proposed approach is first applied on the diagnosis of a civil jet engine gearbox. The vibration signals are part of the publicly available data displayed during the international conference Surveillance 8 held in Roanne in 2015, where a comprehensive feedback can be found in [68]. Two exercises were given to the contestants to benchmark their method of vibration-based diagnosis of rolling-element bearings in non-stationary operating conditions. The data used is recorded from a complex system comprising two main shafts and an accessory gearbox. The signal corresponds to 100 s of a vibration signal recorded during a run-up procedure where the rotational speed of shaft L4 $f_{L4}(t)$ goes from 180 Hz to 240 Hz.

The rotational speed of shaft L4 was provided with a tachometer, recorded simultaneously with the acceleration signal. The recorded vibration signal 'Acc2' contains impulsive events associated with a bearing fault on shaft L5. The damage on the roller bearing is a wide spalled area of 32° in the outer race. The rolling-element bearing has $Z = 18$ rolling elements. Since the impulsive event of interest is related to a fault located on the outer race, the CoR for this fault is the relative rotation between the cage and the outer race of shaft L_5. In what follows, spectra synchronised with either the rotation of shaft L4 f_{L4} or to the relative rotation of the cage $f_{C/O}$ will be shown superimposed, with angular frequency axes scaled according to the relationship between the two order domains in the case of perfect rolling. The theoretical fault frequency is $BPFO = 7.8862 f_{L4} = Z f_{C/O}$ with $Z = 18$. Similarly, the meshing frequency between shaft L5 and L6 is $f_m = 31.5082 f_{L4} = 71.9165 f_{C/O}$. The envelope signal is obtained from the filtered signal between 5 and 12 kHz, which was found after trial-and-error approach to be a good candidate for envelope demodulation. The envelope is then resampled with the tacho signal provided in the contest. The instantaneous phase used for resynchronisation is extracted from the unwrapped phase of narrowband analytic signal with bandwidth of 1.5 events per revolution of shaft $L4$ and centred around the maximum amplitude peak around the expected fault angle frequency, that is $BPFO = Z f_{C/O}$. The phase of the relative rotation between the cage and the outer race is extracted from the method previously described in section 2.3.2.

Figures 16 and 17 present the Fourier transform of envelopes synchronised with the phase of the shaft L4 and with that of relative cycle. The results are presented in the order domain of relative cycle $f_{C/O}$. The bearing synchronised spectrum shows less prominent peaks except at the frequencies associated with the bearing fault. The degradation of the other peaks in the spectrum is caused by the CoR of the bearing being solely synchronous with impulsive events from the outer race of bearing L5. Concerning the spectrum synchronised with the shaft angle, the geared transmission allows the unique cycle of shaft L4 to be synchronous with every shafts-related sources of the gearbox.

Figure 17 displays a detailed view of the spectra around the first and second harmonics of the fault frequency. The spectrum synchronised with respect to the bearing phase exhibits peaks located exactly at multiples of the number

of rolling elements. The comparison of the two spectra shows the two characteristics of cumulative jitter previously described. First, the mean frequencies of the two different peaks associated with the fault are slightly shifted. The shift between the original and synchronised BPFO peaks is found to be the same (0.96%) for the first two harmonics. Second, the distribution of the peaks synchronised with the shaft are spread out on multiple frequency bins compared to the CoR order tracked signal. The use of the phase of the impulses correctly handled the pseudo cyclostationary behaviour of the bearing fault, so that the peak distribution is refocused on a few frequency bins, echoing to the term *spectral sharpener* of Bonnardot [69]. Concerning the amplitude of the peaks of the two different synchronisation schemes, the harmonics of the fault are enhanced with the ratio $R_1 = 0.132/0.037 = 3.57$ for the first harmonic and $R_2 = 0.020/0.012 = 1.67$ for the second.

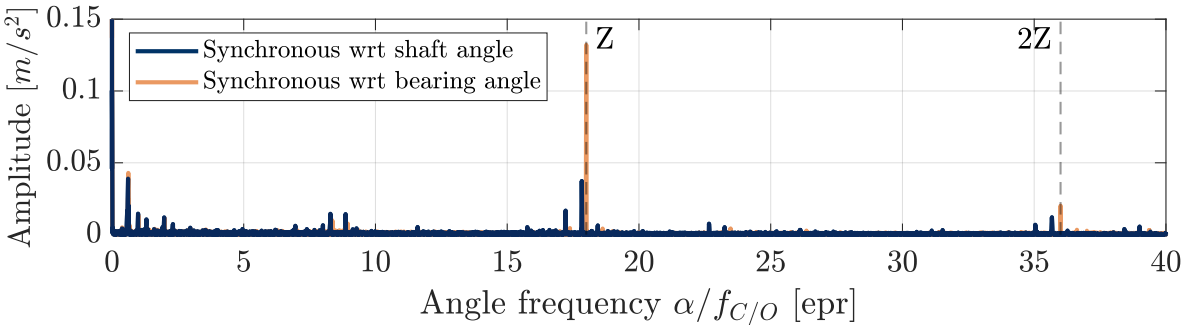

Figure 16: Spectrum of the envelope, synchronised with the tachometer shaft phase (blue) and the relative phase between the cage and the outer race (orange), expressed in the order domain relative to $f_{C/O}$.

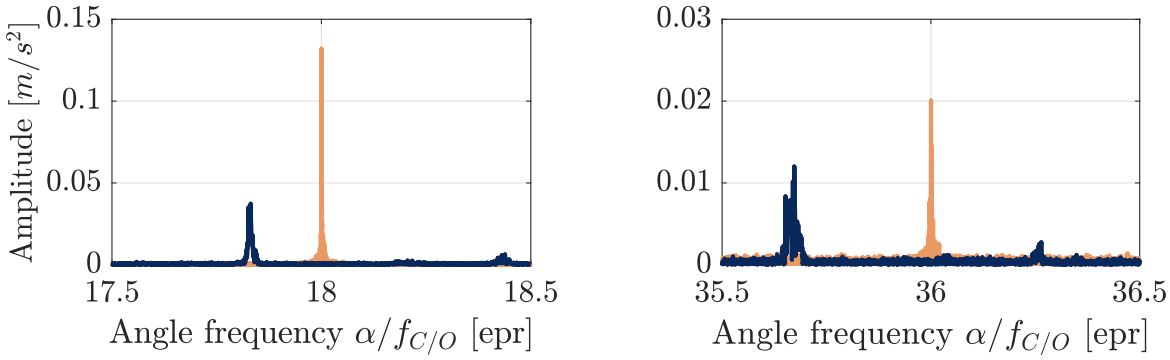

Figure 17: Spectra of the envelope, around the fault frequency (a) and its second harmonic (b). The colours refers to the legend of Fig. 16.

To highlight that the method does not simply offer a better estimation compared to the tacho signal, Fig. 18 presents the Fourier spectrum of the raw signal synchronised either with respect to the phase of shaft L4 (blue) or to the bearing phase (orange), where the x-axis now represents events per revolution of the L4 shaft. A clear and narrow peak is located at the meshing frequency f_m for the shaft synchronised signal but is completely smeared out around f_m with the bearing synchronised signal. On the other hand, the third harmonic of the fault frequency at $3BPFO = 23.6586 f_{L4}$ is brought out in the re-synchronised spectrum. Again, this highlight the fact that the signal incorporates periodic events with different CoR whether they are generated by rotations synchronous with the shaft rotation for the meshing or synchronous with the relative rotation of the cage for the bearing fault. For events synchronous with shafts revolutions, the choice of a particular CoR to monitor the entire gearbox, like here with the rotation of L4, is inconsequential as long as the rotations are kinematically bound by geared transmission. For jittered events such as bearings, new references for synchronisation are needed to restore their cyclostationarity. This

particular aspect limits a simple application of spectral sparsity measures for complex signals with multiples sources. In the frequency band presented in Fig. 16, the Hoyer index of both spectra is calculated. The Hoyer index [70] is a normalised version of the l_2/l_1 norm sparsity measure. The envelope spectrum synchronised with respect to the bearing angle is sparser with the Hoyer index being 0.74 against 0.71 for the shaft one. Since the envelope spectrum is dominated by bearing-related contributions, the resynchronisation improved the sparsity of the spectrum. Concerning the spectrum of the signal of Fig. 18, the shaft synchronised spectrum is sparser than the bearing one with respective Hoyer indexes of 0.65 and 0.41. The spectrum is dominated by meshing frequencies synchronous with the shafts. Locally, the spectral sparsity of bearing-related frequencies is improved with a visible sharpening of fault frequencies. However, this comes at the expense of a degradation of shaft-related peaks, decreasing the global spectral sparsity measure.

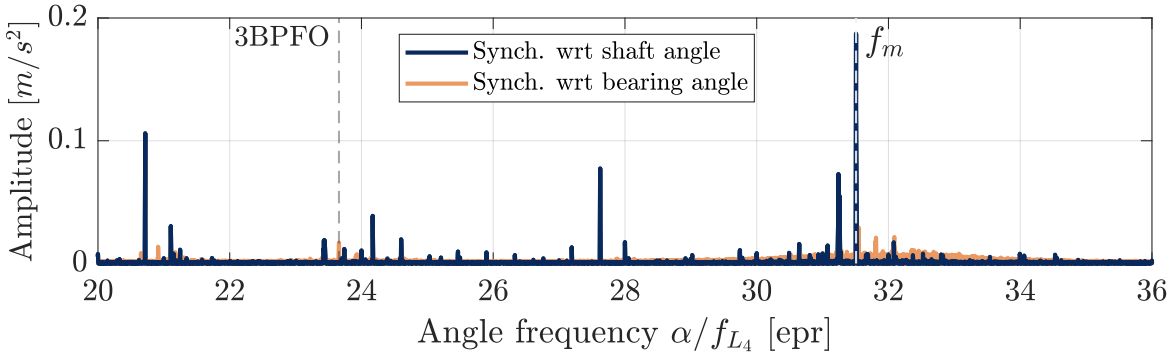

Figure 18: Spectrum of the raw signal, synchronised with the tachometer shaft phase (blue) and the relative phase between the cage and the outer race (orange), expressed in the order domain relative to f_{L4}.

3.2.2. Application to the monitoring of a bearing wind turbine

The proposed approach is tested on the data from an industrial wind turbine of 2 MW monitored for approximately a year by the company Engie Green. The kinematics of the gearbox is provided in Fig. 19. The main shaft supporting the blades is shown in red and the function of the system is to increase the rotational speed from the main shaft to the high-speed shaft (HSS), carrying gear No. 7 shown in olive, for the generator. During a year of observation, a fault on the inner race of the bearing labelled K appeared and worsen until its replacement. The faulty bearing is a FAG N2234E with $Z = 17$ rolling elements and a fault frequency of $BPFI = 9.83 f_{\mathrm{HSS}}$. The meshing frequency between gears No. 6 and No. 7 is $f_m = 29 f_{\mathrm{HSS}}$.

An accelerometer is placed in the vicinity of the High-Speed Shaft (HSS) and records associated vibration signals during normal operation of the machine. All the signals are recorded during 10 s sampled at 20 kHz, and quantified with a 12 bits resolution. To limit the effect of varying loading, the signals are recorded for similar operating conditions. Being dependent on the external wind conditions, the signals are not recorded with a constant inter-time interval. In the presented work, the records are labelled with a numerical index, where the total duration of the monitoring spans approximately a year. The bearing was replaced during maintenance operation after signal index 54. Figure 20 shows the inner ring of the bearing with the fault. A spall of diameter 3mm was located on the inner ring. Rolling elements and outer ring were found to be undamaged under inspection.

For each record, the envelope of the signal is obtained by filtering it between 5 and 10 kHz. Then, the envelope is resampled using the shaft angle obtained by demodulation of the meshing frequency $f_m = 29 f_{\mathrm{HSS}}$ between gears No. 6 and No. 7. A narrowband filter of 1.8 epr of shaft angle was found by trial and error to achieve good results for the demodulation of the bearing phase. The extracted instantaneous speed is proportional to the relative speed between the cage and the inner race $BPFI = Z f_{C/I}$ and used below for signal synchronisation.

Figures 21 and 22 compare respectively the envelope spectrum of signal index 1 and 54, synchronous with the shaft phase (blue) and with the estimated bearing phase (orange). The spectra have been normalised to the maximum peak amplitude of the BPFI peak for all the recorded signals, occurring for signal index 48. Starting with Fig. 21, the demodulation created a peak at the expected fault frequency. To assess whether this peak is an artefact or not,

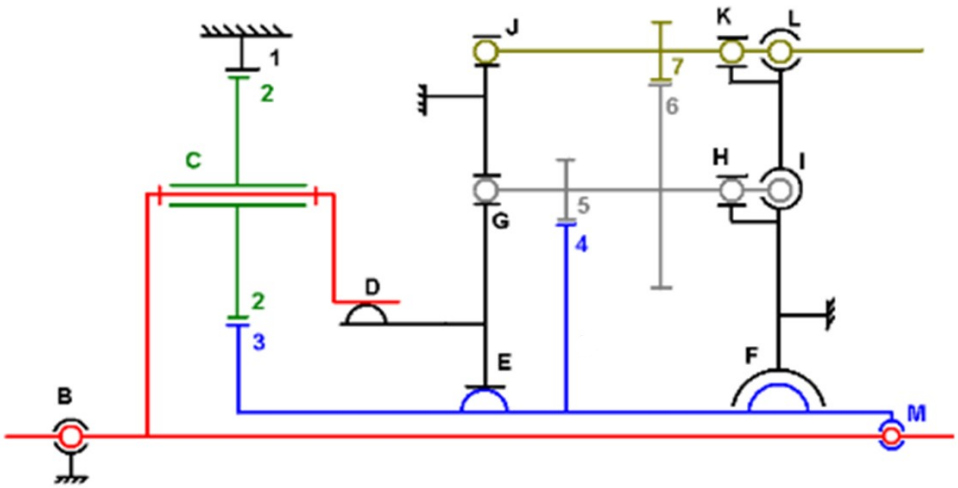

Figure 19: Kinematics of the wind turbine gearbox.

(a) (b)

Figure 20: (a) Inner ring of the faulty bearing with (b) a detailed view on the spall. The spall diameter is 3mm.

the confidence test of Appendix A is done. The threshold for the rayleigh-ness test on the demodulation band gives $\nu_x = -0.0019$ for a 1 % false-alarm probability, while the testing variable is $x = -0.0047$. The spurious peak could have also been detected qualitatively. Indeed, the second harmonic is absent as well as modulation bands, expected for this kind of fault. Comparatively on Fig. 22, The resynchronisation successfully narrows the BPFI peak that was previously spread out by the cumulative jitter. The fault being localised on the inner shaft, the impulses are modulated by the rotation of the shaft at 1 event per revolution of the HSS. Sidebands of 1 epr around the BPFI peak can be observed as well as peaks at 1 epr and higher harmonics. The second harmonic is enhanced as well. The rayleigh-ness test in this case yields values of $\nu_x = 94$ and $x = 10515$ for a 1% false-alarm probability. The synchronisation to bearing angle showed enhanced amplitude for all the related events, that is not only at the BPFI peaks, but also for the modulations.

Figure 23 presents the amplitude of the BPFI peak synchronised to shaft angle and the bearing one during approximately a year of operation. The amplitude of the peak is taken as the maximum within a small band around the expected frequency to account for the offset. A moving average curve using 5 data-points is additionally shown in dotted line. For each signal, a confidence test on the rayleigh-ness of the demodulation band was applied with a 1 % false-alarm probability. The rejection of the hypothesis on the presence of a harmonic component is shown with the voided squares. For the first signals recorded, the hypothesis is rejected, the machine is fault-free and the amplitude

corresponds to the maximum of the random noise within the band. However, from index 11, the amplitude of the signal is rising progressively as the fault extends. The synchronised amplitudes in orange show distinct features from the original one. First, all the signals synchronised to the bearing angle show greater amplitude compared to the original one, highlighting that the synchronisation narrowed the peak distribution caused by the jitter. The amplitude of the peak is supposedly more representative of the mechanical energy delivered by the impulses. Second, the dispersion away from the moving average is less important for the resynchronised signal. As explained before, the spread of the peak distribution is dependent on the non-cumulative jitter which can be influenced by external various factors. The reduction of variability previously caused by the non-cumulative jitter permits better fault gravity trending as the amplitude of the peak is less dependent on external uncontrolled conditions influencing the jitter. The remaining variability in the synchronised signals can be explained by other external conditions such as operating speed or active power during the recording.

Figure 24 presents the amplitude difference between the original and resynchronised signals. As for the previous figure, the rejection of the rayleigh-ness test is shown with the voided circles. For the first 10 samples the bearing is supposedly healthy, there is no peak associated with a cyclic event. The difference between the two amplitude-based spectral indicators are caused by the artefact described in section 3.1. From index 20, the difference shows an increasing trend with greater dispersion. In our opinion, this highlights the fact that the spreading law of the peak distribution is changing with the growth of the fault. In short, with the fault extending, it will tend to increase the non-cumulative jitter and more mechanical energy will be delivered. The latter aspect will increase the amplitude of the peak, but the former will broaden the distribution. Restoring the cyclicity of faulty bearing signals has multiple benefits for condition monitoring. From a diagnosis point of view, the spectral signature will be easier to interpret, with highlighted harmonics and modulation band. The presented experimental case is not sufficient to settle the early detection issue. The main advantage of using the appropriate cycle of reference is in our opinion on the concentration of the mechanical energy independently on jitter intensity, that will permit a better trending and assessment on the evolution of the gravity of the fault.

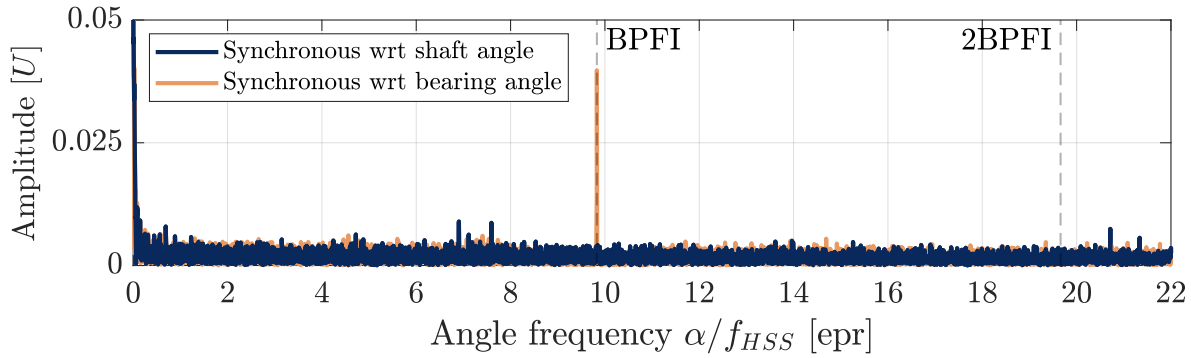

Figure 21: Spectrum of the envelope of signal index 1, synchronised with the shaft phase (blue) and the estimated relative phase between the cage and the inner race (orange), expressed in the order domain relative to f_{HSS}.

4. Conclusion

This paper has proposed an in-depth study of pseudo-cyclostationary properties of faulty bearing signals. The principle of using the angle-time relationship of a CoR to restore cyclostationary for gear-related signals has been reminded. The train of impulses generated by bearing faults is known to be slightly asynchronous with the race's rotation. The uncertainty of instants of impact described by the jitter causes the train of impulses to be pseudo-cyclostationary when viewed as a function of shaft rotations. The jitter can be explained by the normal operation of the bearing, varying contact angle and the hypothetical presence of a fault.

New CoR synchronous with bearing-related events have been described. A method to demodulate the phase of the train of impulses has been shown to be very similar to the methods used for shaft demodulation. Based on the point process models and observations in the spectra, the use of the phase of the impulses for resampling has shown to

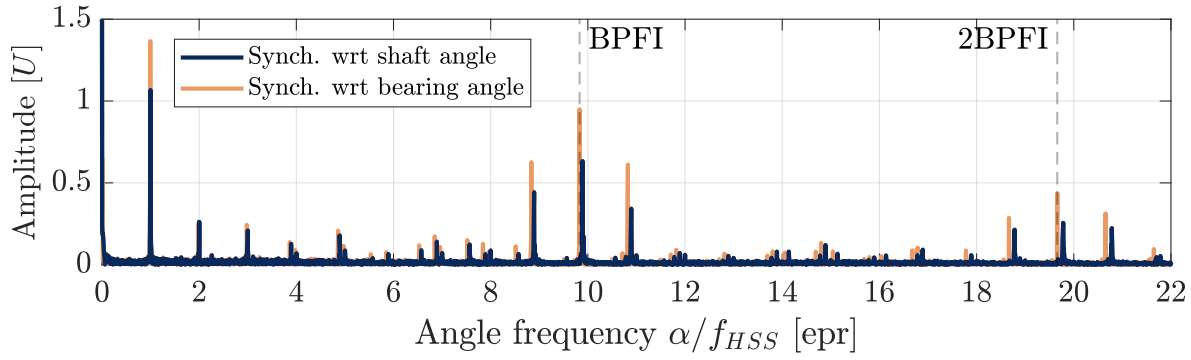

Figure 22: Spectrum of the envelope of signal index 54, synchronised with the shaft phase (blue) and the estimated relative phase between the cage and the inner race (orange), expressed in the order domain relative to f_{HSS}.

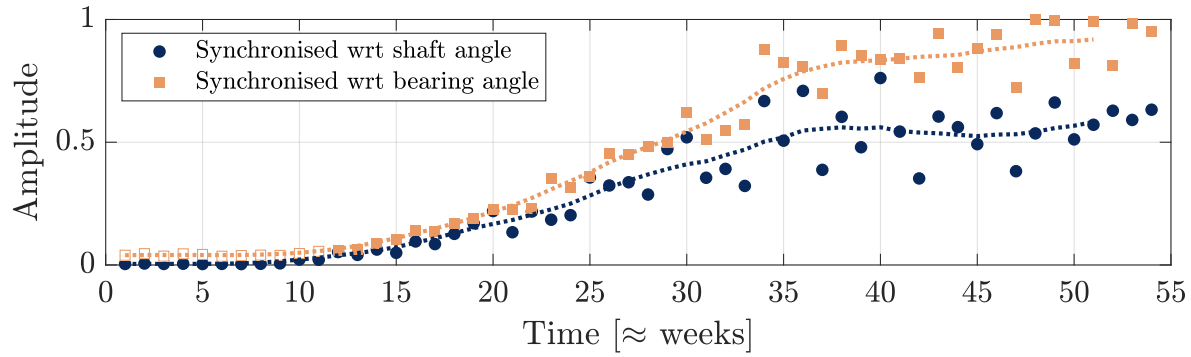

Figure 23: Amplitude of BPFI peak, taken in the spectrum either synchronised with the shaft phase (blue) or with the bearing phase (orange). The peak amplitude is taken as the maximum within a narrowband frequency band around the expected fault frequency.

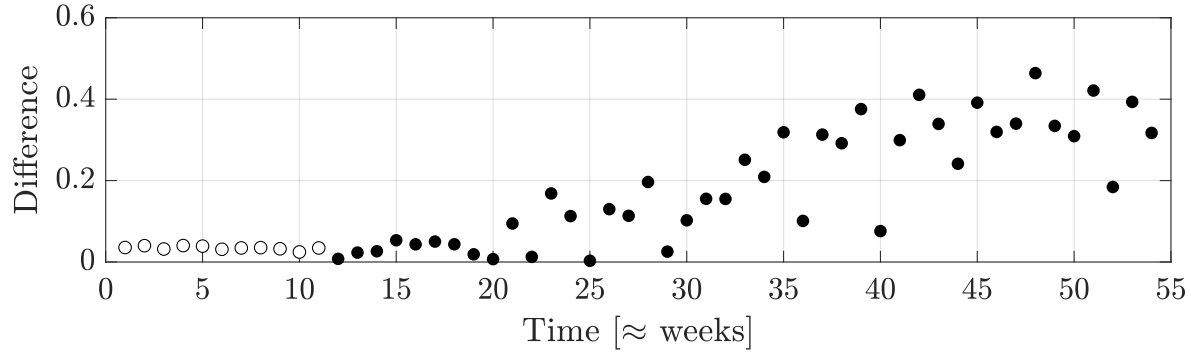

Figure 24: Difference between the two amplitude indicators of Fig. 23.

successfully restore cyclostationarity. Two original contributions about the effect of narrowband filter bandwidth and the introduction of the artefact have been thoroughly explained and put the capacities of the method into perspective. The method has been tested on numerical and two industrial applications. The key findings are

- The cyclostationarity of train of impulses generated by bearings faults can be restored provided that the signal is synchronised with respect to new CoR, differing from the shaft cycles.
- Synchronising the signals from the phase of the envelope will handle the effects of cumulative jitter, but is likely to create residual non-cumulative jitter.

- For methods based on the demodulation of the analytical signal, the bandwidth of the narrowband filter influences the precision of phase reconstruction.
- Artefacts are generated when the method blindly applies to a random signal, which can lead to erroneous diagnostic.
- An hypothesis test is designed to ensure the presence of a cyclic event. The method is robust against poorly synchronised signals.
- A run-to-failure industrial study of a wind turbine bearing highlights the superiority of using resynchronised signals for monitoring.

Synchronising the signals with respect to the bearing cycle restores cyclostationarity and opens doors for tools that were dedicated to gear monitoring. As such, further work will focus on the application of synchronous average schemes.

Appendix A. Threshold derivation

The statistical test is based on the work of Giunta and Vandendorpe [66]. More details can be found in this reference but the key steps are reminded here. The goal is to test whether a real positive series $\Gamma = \{|R_1|, ..., |R_k|\}$ is, H_0, a realisation of Rayleigh-distributed random process ($R_k = \mu + \epsilon_k$, where R_k follows a complex Gaussian model, with $\mu = 0$) against H_1, the hypothesis of a Rice-distributed random process ($\mu \neq 0$). The testing variable is

$$x = 2\left[\frac{1}{K}\sum_{k=1}^{K}|R_k|^2\right]^2 - \frac{1}{K}\sum_{k=1}^{K}|R_k|^4, \tag{A.1}$$

with expected value

$$\mathrm{E}[x] = \mu^4 + 2(3-\alpha)\sigma^2 + \frac{2}{K}[4\mu^2\sigma^2 + 2(\alpha-1)\sigma^4], \tag{A.2}$$

and variance

$$\mathrm{var}[x] \approx \frac{16}{K}\mu^6\sigma^2 + \frac{88-24\alpha}{K}\mu^4\sigma^4 + \frac{128-80\alpha+16\beta}{K}\mu^2\sigma^6 + \frac{-68+2\alpha^2+88\alpha-24\beta+2\gamma}{K}\sigma^8, \tag{A.3}$$

where σ^2, α, β and γ are respectively the marginal moments of order $2, 4, 6$ and 8. The test threshold is tuned for a fixed probability of false alarm P_{fa} as

$$\nu_x = \mathrm{E}[x]|_{H_0} + (2\mathrm{var}[x]|_{H_0})^{1/2}\mathrm{erf}^{-1}(1-2P_{\mathrm{fa}}), \tag{A.4}$$

where the expected value and variance can be calculated from the previous equations with $\mu = 0$.

Acknowledgements

This work was supported by the LABEX CeLyA (Grant No. ANR-10-LABX-0060) of Universite de Lyon, within the program "Investissements d'Avenir" (Grant No. ANR16-IDEX-0005) operated by the French National Research Agency (ANR).

References

[1] D.-Y. Kim, H.-B. Yun, S.-M. Yang, W.-T. Kim, D.-P. Hong, Fault diagnosis of ball bearings within rotational machines using the infrared thermography method, Journal of the Korean Society for Nondestructive Testing 30 (6) (2010) 558–563, publisher: The Korean Society for Nondestructive Testing.

[2] J. M. Wakiru, L. Pintelon, P. N. Muchiri, P. K. Chemweno, A review on lubricant condition monitoring information analysis for maintenance decision support, Mechanical Systems and Signal Processing 118 (2019) 108–132. doi:10.1016/j.ymssp.2018.08.039.
URL https://linkinghub.elsevier.com/retrieve/pii/S0888327018305788

[3] W. T. Thomson, I. Culbert, Current Signature Analysis for Condition Monitoring of Cage Induction Motors: Industrial Application and Case Histories, John Wiley & Sons, Inc., Hoboken, NJ, USA, 2016. doi:10.1002/9781119175476.
URL http://doi.wiley.com/10.1002/9781119175476

[4] S. M. A. Al-Obaidi, M. S. Leong, R. R. Hamzah, A. M. Abdelrhman, A Review of Acoustic Emission Technique for Machinery Condition Monitoring: Defects Detection & Diagnostic, Applied Mechanics and Materials 229-231 (2012) 1476–1480. doi:10.4028/www.scientific.net/AMM.229-231.1476.
URL https://www.scientific.net/AMM.229-231.1476

[5] H. Andre, A. Bourdon, D. Rémond, On the use of the Instantaneous Angular Speed measurement in non-stationary mechanism monitoring, in: ASME 2011 International Design Engineering Technical Conferences, Washington, United States, 2011, pp. DETC2011/MECH–47470.
URL https://hal.archives-ouvertes.fr/hal-00694854

[6] D. Wang, K.-L. Tsui, Q. Miao, Prognostics and Health Management: A Review of Vibration Based Bearing and Gear Health Indicators, IEEE Access 6 (2018) 665–676, conference Name: IEEE Access. doi:10.1109/ACCESS.2017.2774261.

[7] D. Wang, Some further thoughts about spectral kurtosis, spectral L2/L1 norm, spectral smoothness index and spectral Gini index for characterizing repetitive transients, Mechanical Systems and Signal Processing 108 (2018) 360–368. doi:10.1016/j.ymssp.2018.02.034.
URL https://www.sciencedirect.com/science/article/pii/S0888327018300979

[8] C. Peeters, J. Antoni, J. Helsen, Blind filters based on envelope spectrum sparsity indicators for bearing and gear vibration-based condition monitoring, Mechanical Systems and Signal Processing 138 (2020) 106556. doi:10.1016/j.ymssp.2019.106556.
URL https://www.sciencedirect.com/science/article/pii/S0888327019307770

[9] Y. Miao, J. Wang, B. Zhang, H. Li, Practical framework of Gini index in the application of machinery fault feature extraction, Mechanical Systems and Signal Processing 165 (2022) 108333. doi:10.1016/j.ymssp.2021.108333.
URL https://linkinghub.elsevier.com/retrieve/pii/S0888327021006919

[10] P. D. McFadden, Interpolation techniques for time domain averaging of gear vibration, Mechanical Systems and Signal Processing 3 (1) (1989) 87–97. doi:10.1016/0888-3270(89)90024-1.
URL https://www.sciencedirect.com/science/article/pii/0888327089900241

[11] C. Peeters, Q. Leclère, J. Antoni, P. Lindahl, J. Donnal, S. Leeb, J. Helsen, Review and comparison of tacholess instantaneous speed estimation methods on experimental vibration data, Mechanical Systems and Signal Processing 129 (2019) 407–436. doi:10.1016/j.ymssp.2019.02.031.
URL https://linkinghub.elsevier.com/retrieve/pii/S0888327019301153

[12] J. Antoni, Cyclic spectral analysis of rolling-element bearing signals: Facts and fictions, Journal of Sound and Vibration 304 (3-5) (2007) 497–529. doi:10.1016/j.jsv.2007.02.029.
URL https://linkinghub.elsevier.com/retrieve/pii/S0022460X07001551

[13] P. D. Mcfadden, M. M. Toozhy, APPLICATION OF SYNCHRONOUS AVERAGING TO VIBRATION MONITORING OF ROLLING ELEMENT BEARINGS, Mechanical Systems and Signal Processing 14 (6) (2000) 891–906. doi:10.1006/mssp.2000.1290.
URL https://www.sciencedirect.com/science/article/pii/S0888327000912901

[14] E. P. Sabini, J. A. Lorenc, O. Henyan, K. L. Hauenstein, Bearing defect detection using time synchronous averaging (TSA) of an enveloped accelerometer signal (Jan. 2004).
URL https://patents.google.com/patent/US6681634B2/en

[15] D. Siegel, H. Al-Atat, V. Shauche, L. Liao, J. Snyder, J. Lee, Novel method for rolling element bearing health assessment—A tachometerless synchronously averaged envelope feature extraction technique, Mechanical Systems and Signal Processing 29 (2012) 362–376. doi:10.1016/j.ymssp.2012.01.003.
URL https://www.sciencedirect.com/science/article/pii/S0888327012000040

[16] M. Zhao, J. Lin, X. Xu, Y. Lei, Tacholess Envelope Order Analysis and Its Application to Fault Detection of Rolling Element Bearings with Varying Speeds, Sensors 13 (8) (2013) 10856–10875, number: 8 Publisher: Multidisciplinary Digital Publishing Institute. doi:10.3390/s130810856.
URL https://www.mdpi.com/1424-8220/13/8/10856

[17] C. Yan, M. Zhao, J. Lin, K. Liang, Zhiqiang Zhang, Fault signature enhancement and skidding evaluation of rolling bearing based on estimating the phase of the impulse envelope signal, Journal of Sound and Vibration 485 (2020) 115529. doi:10.1016/j.jsv.2020.115529.
URL https://linkinghub.elsevier.com/retrieve/pii/S0022460X20303618

[18] C. Yan, J. Lin, K. Liang, Z. Ma, Z. Zhang, Tacholess skidding evaluation and fault feature enhancement base on a two-step speed estimation method for rolling bearings, Mechanical Systems and Signal Processing 162 (2022) 108017. doi:10.1016/j.ymssp.2021.108017.
URL https://linkinghub.elsevier.com/retrieve/pii/S088832702100412X

[19] T. Wang, M. Liang, J. Li, W. Cheng, Rolling element bearing fault diagnosis via fault characteristic order (FCO) analysis, Mechanical Systems and Signal Processing 45 (1) (2014) 139–153. doi:10.1016/j.ymssp.2013.11.011.
URL https://linkinghub.elsevier.com/retrieve/pii/S0888327013006389

[20] T. Wang, F. Chu, Bearing fault diagnosis under time-varying rotational speed via the fault characteristic order (FCO) index based demodulation and the stepwise resampling in the fault phase angle (FPA) domain, ISA Transactions 94 (2019) 391–400. doi:10.1016/j.isatra.2019.04.020.
URL https://www.sciencedirect.com/science/article/pii/S0019057819301946

[21] S. Lu, X. Wang, Q. He, F. Liu, Y. Liu, Fault diagnosis of motor bearing with speed fluctuation via angular resampling of transient sound signals, Journal of Sound and Vibration 385 (2016) 16–32. doi:10.1016/j.jsv.2016.09.012.
URL https://www.sciencedirect.com/science/article/pii/S0022460X16304771

[22] H. Zhang, P. Borghesani, W. A. Smith, R. B. Randall, M. R. Shahriar, Z. Peng, Tracking the natural evolution of bearing spall size using cyclic natural frequency perturbations in vibration signals, Mechanical Systems and Signal Processing 151 (2021) 107376. doi:10.1016/j.ymssp.2020.107376.

URL https://linkinghub.elsevier.com/retrieve/pii/S0888327020307627
[23] J. Antoni, F. Bonnardot, A. Raad, M. El Badaoui, Cyclostationary modelling of rotating machine vibration signals, Mechanical Systems and Signal Processing 18 (6) (2004) 1285–1314. doi:10.1016/S0888-3270(03)00088-8.
URL https://linkinghub.elsevier.com/retrieve/pii/S0888327003000888
[24] P. D. McFadden, J. D. Smith, Model for the vibration produced by a single point defect in a rolling element bearing, Journal of Sound and Vibration 96 (1) (1984) 69–82. doi:10.1016/0022-460X(84)90595-9.
URL https://www.sciencedirect.com/science/article/pii/0022460X84905959
[25] M. Cerrada, R.-V. Sánchez, C. Li, F. Pacheco, D. Cabrera, J. Valente de Oliveira, R. E. Vásquez, A review on data-driven fault severity assessment in rolling bearings, Mechanical Systems and Signal Processing 99 (2018) 169–196. doi:10.1016/j.ymssp.2017.06.012.
URL https://www.sciencedirect.com/science/article/pii/S0888327017303242
[26] P. D. Mcfadden, DETECTION OF GEAR FAULTS BY DECOMPOSITION OF MATCHED DIFFERENCES OF VIBRATION SIGNALS, Mechanical Systems and Signal Processing 14 (5) (2000) 805–817. doi:10.1006/mssp.2000.1318.
URL https://www.sciencedirect.com/science/article/pii/S0888327000913189
[27] D. Rémond, J. Antoni, R. B. Randall, Instantaneous Angular Speed (IAS) processing and related angular applications, Mechanical Systems and Signal Processing 45 (1) (2014) 24–27. doi:10.1016/j.ymssp.2013.10.015.
URL https://www.sciencedirect.com/science/article/pii/S0888327013005189
[28] Q. Leclère, L. Pruvost, E. Parizet, Angular and temporal determinism of rotating machine signals: The diesel engine case, Mechanical Systems and Signal Processing 24 (7) (2010) 2012–2020. doi:10.1016/j.ymssp.2010.05.006.
URL https://www.sciencedirect.com/science/article/pii/S0888327010001494
[29] D. Abboud, J. Antoni, M. Eltabach, S. Sieg-Zieba, Angle-time cyclostationarity for the analysis of rolling element bearing vibrations, Measurement 75 (2015) 29–39. doi:10.1016/j.measurement.2015.07.017.
URL https://www.sciencedirect.com/science/article/pii/S0263224115003528
[30] F. Bonnardot, M. El Badaoui, R. Randall, J. Danière, F. Guillet, Use of the acceleration signal of a gearbox in order to perform angular resampling (with limited speed fluctuation), Mechanical Systems and Signal Processing 19 (4) (2005) 766–785. doi:10.1016/j.ymssp.2004.05.001.
URL https://linkinghub.elsevier.com/retrieve/pii/S0888327004000664
[31] R. B. Randall, J. Antoni, Rolling element bearing diagnostics—A tutorial, Mechanical Systems and Signal Processing 25 (2) (2011) 485–520. doi:10.1016/j.ymssp.2010.07.017.
URL https://www.sciencedirect.com/science/article/pii/S0888327010002530
[32] J. E. Shigley, C. R. Mischke, T. H. Brown (Eds.), Standard handbook of machine design, 3rd Edition, McGraw-Hill, New York, 2004.
[33] I. Howard, A Review of Rolling Element Bearing Vibration 'Detection, Diagnosis and Prognosis',, Tech. rep., DEFENCE SCIENCE AND TECHNOLOGY ORGANIZATION CANBERRA (AUSTRALIA), section: Technical Reports (Oct. 1994).
URL https://apps.dtic.mil/sti/citations/ADA291123
[34] J. I. Taylor, Identification of Bearing Defects by Spectral Analysis, Journal of Mechanical Design 102 (2) (1980) 199–204. doi:10.1115/1.3254730.
URL https://doi.org/10.1115/1.3254730
[35] C. Springer, The effects of internal geometry changes on the frequencies generated by deep groove ball bearings, Tappi journal 73 (5) (1990) 101–105, publisher: Technical Association of the Pulp and Paper Industry.
[36] P. Borghesani, R. Ricci, S. Chatterton, P. Pennacchi, A new procedure for using envelope analysis for rolling element bearing diagnostics in variable operating conditions, Mechanical Systems and Signal Processing 38 (1) (2013) 23–35. doi:10.1016/j.ymssp.2012.09.014.
URL https://www.sciencedirect.com/science/article/pii/S088832701200372X
[37] P. Pennacchi, P. Borghesani, S. Chatterton, R. Ricci, An experimental based assessment of the deviation of the bearing characteristic frequencies, in: proceedings of the 6th International Conference Acoustic and Vibratory Surveillance Methods and Diagnostic Techniques, Institute of Technology of Chartres, 2011, pp. 1–8.
[38] P. K. Gupta, Generalized dynamic simulation of skid in ball bearings, Journal of Aircraft 12 (4) (1975) 260–265, publisher: American Institute of Aeronautics and Astronautics _eprint: https://doi.org/10.2514/3.44442. doi:10.2514/3.44442.
URL https://doi.org/10.2514/3.44442
[39] N. T. Liao, J. F. Lin, Ball bearing skidding under radial and axial loads, Mechanism and Machine Theory 37 (1) (2002) 91–113, publisher: Elsevier.
[40] E. Laniado-Jacome, J. Meneses-Alonso, V. Diaz-Lopez, A study of sliding between rollers and races in a roller bearing with a numerical model for mechanical event simulations, Tribology International 43 (11) (2010) 2175–2182, publisher: Elsevier.
[41] Y. Wang, W. Wang, S. Zhang, Z. Zhao, Investigation of skidding in angular contact ball bearings under high speed, Tribology International 92 (2015) 404–417, publisher: Elsevier.
[42] Y. Liu, Z. Chen, L. Tang, W. Zhai, Skidding dynamic performance of rolling bearing with cage flexibility under accelerating conditions, Mechanical Systems and Signal Processing 150 (2021) 107257. doi:10.1016/j.ymssp.2020.107257.
URL https://www.sciencedirect.com/science/article/pii/S0888327020306439
[43] H. Luo, H. Qiu, G. Ghanime, M. Hirz, G. van der Merwe, Synthesized Synchronous Sampling Technique for Differential Bearing Damage Detection, Journal of Engineering for Gas Turbines and Power 132 (7) (2010) 072501. doi:10.1115/1.4000092.
URL https://asmedigitalcollection.asme.org/gasturbinespower/article/doi/10.1115/1.4000092/408787/Synthesized-Synchronous-Sampling-Technique-for
[44] A. Moazen-ahmadi, C. Q. Howard, A defect size estimation method based on operational speed and path of rolling elements in defective bearings, Journal of Sound and Vibration 385 (2016) 138–148. doi:10.1016/j.jsv.2016.09.014.
URL https://www.sciencedirect.com/science/article/pii/S0022460X16304795
[45] A. Moazen Ahmadi, C. Q. Howard, D. Petersen, The path of rolling elements in defective bearings: Observations, analysis and methods to estimate spall size, Journal of Sound and Vibration 366 (2016) 277–292. doi:10.1016/j.jsv.2015.12.011.

URL https://www.sciencedirect.com/science/article/pii/S0022460X15009931
[46] S. Singh, U. G. Köpke, C. Q. Howard, D. Petersen, Analyses of contact forces and vibration response for a defective rolling element bearing using an explicit dynamics finite element model, Journal of Sound and Vibration 333 (21) (2014) 5356–5377. doi:10.1016/j.jsv.2014.05.011.
URL https://www.sciencedirect.com/science/article/pii/S0022460X14004015
[47] T. A. Harris, An Analytical Method to Predict Skidding in High Speed Roller Bearings, A S L E Transactions 9 (3) (1966) 229–241, publisher: Taylor & Francis _eprint: https://doi.org/10.1080/05698196608972139. doi:10.1080/05698196608972139.
URL https://doi.org/10.1080/05698196608972139
[48] J. Antoni, R. B. Randall, A Stochastic Model for Simulation and Diagnostics of Rolling Element Bearings With Localized Faults, Journal of Vibration and Acoustics 125 (3) (2003) 282–289. doi:10.1115/1.1569940.
URL https://doi.org/10.1115/1.1569940
[49] R. B. Randall, J. Antoni, S. Chobsaard, THE RELATIONSHIP BETWEEN SPECTRAL CORRELATION AND ENVELOPE ANALYSIS IN THE DIAGNOSTICS OF BEARING FAULTS AND OTHER CYCLOSTATIONARY MACHINE SIGNALS, Mechanical Systems and Signal Processing 15 (5) (2001) 945–962. doi:10.1006/mssp.2001.1415.
URL https://www.sciencedirect.com/science/article/pii/S0888327001914153
[50] J. Antoni, R. B. Randall, Differential Diagnosis of Gear and Bearing Faults, Journal of Vibration and Acoustics 124 (2) (2002) 165–171. doi:10.1115/1.1456906.
URL https://doi.org/10.1115/1.1456906
[51] S. Elton, Jitter identification techniques for a regular event-based process, in: 1999 IEEE International Conference on Acoustics, Speech, and Signal Processing. Proceedings. ICASSP99 (Cat. No.99CH36258), Vol. 5, 1999, pp. 2801–2804 vol.5, iSSN: 1520-6149. doi:10.1109/ICASSP.1999.761344.
[52] P. Borghesani, W. A. Smith, R. B. Randall, J. Antoni, M. El Badaoui, Z. Peng, Bearing signal models and their effect on bearing diagnostics, Mechanical Systems and Signal Processing 174 (2022) 109077. doi:10.1016/j.ymssp.2022.109077.
URL https://www.sciencedirect.com/science/article/pii/S0888327022002473
[53] H. E. Staph, W. A. Gunkel, G. F. Munsch, Bearing test assembly with rotary cage follower (Jun. 1967).
URL https://patents.google.com/patent/US3324708/en
[54] R. Randall, W. Smith, Use of the Teager Kaiser Energy Operator to estimate machine speed, PHM Society European Conference 3 (1), number: 1 (2016). doi:10.36001/phme.2016.v3i1.1628.
URL https://www.papers.phmsociety.org/index.php/phme/article/view/1628
[55] J. Antoni, Fast computation of the kurtogram for the detection of transient faults, Mechanical Systems and Signal Processing 21 (1) (2007) 108–124. doi:10.1016/j.ymssp.2005.12.002.
URL https://www.sciencedirect.com/science/article/pii/S0888327005002414
[56] T. Barszcz, A. JabŁoński, A novel method for the optimal band selection for vibration signal demodulation and comparison with the Kurtogram, Mechanical Systems and Signal Processing 25 (1) (2011) 431–451. doi:10.1016/j.ymssp.2010.05.018.
URL https://www.sciencedirect.com/science/article/pii/S0888327010001895
[57] J. Antoni, The infogram: Entropic evidence of the signature of repetitive transients, Mechanical Systems and Signal Processing 74 (2016) 73–94. doi:10.1016/j.ymssp.2015.04.034.
URL https://www.sciencedirect.com/science/article/pii/S0888327015002174
[58] A. Mauricio, K. Gryllias, Cyclostationary-based Multiband Envelope Spectra Extraction for bearing diagnostics: The Combined Improved Envelope Spectrum, Mechanical Systems and Signal Processing 149 (2021) 107150. doi:10.1016/j.ymssp.2020.107150.
URL https://www.sciencedirect.com/science/article/pii/S0888327020305367
[59] A. Mauricio, W. A. Smith, R. B. Randall, J. Antoni, K. Gryllias, Improved Envelope Spectrum via Feature Optimisation-gram (IESFOgram): A novel tool for rolling element bearing diagnostics under non-stationary operating conditions, Mechanical Systems and Signal Processing 144 (2020) 106891. doi:10.1016/j.ymssp.2020.106891.
URL https://www.sciencedirect.com/science/article/pii/S0888327020302776
[60] B. Hou, D. Wang, T. Xia, L. Xi, Z. Peng, K.-L. Tsui, Generalized Gini indices: Complementary sparsity measures to Box-Cox sparsity measures for machine condition monitoring, Mechanical Systems and Signal Processing 169 (2022) 108751. doi:10.1016/j.ymssp.2021.108751.
URL https://www.sciencedirect.com/science/article/pii/S0888327021010670
[61] M. D. Coats, R. B. Randall, Order-Tracking with and without a tacho signal for gear fault diagnostics, 2012, p. 8.
[62] C. Peeters, J. Antoni, Q. Leclère, T. Verstraeten, J. Helsen, Multi-harmonic phase demodulation method for instantaneous angular speed estimation using harmonic weighting, Mechanical Systems and Signal Processing 167 (2022) 108533. doi:10.1016/j.ymssp.2021.108533.
URL https://www.sciencedirect.com/science/article/pii/S088832702100875X
[63] I. Djurović, L. Stanković, An algorithm for the Wigner distribution based instantaneous frequency estimation in a high noise environment, Signal Processing 84 (3) (2004) 631–643. doi:10.1016/j.sigpro.2003.12.006.
URL https://www.sciencedirect.com/science/article/pii/S0165168403003463
[64] S. O. Rice, Mathematical analysis of random noise, The Bell System Technical Journal 23 (3) (1944) 282–332, conference Name: The Bell System Technical Journal. doi:10.1002/j.1538-7305.1944.tb00874.x.
[65] J. L. Lawson, G. E. Uhlenbeck (Eds.), Threshold signals, Threshold signals, McGraw-Hill, New York, NY, US, 1950, pages: 388.
[66] G. Giunta, L. Vandendorpe, A "rayleigh-ness" test for DS/SS code acquisition, IEEE Transactions on Communications 51 (9) (2003) 1492–1501. doi:10.1109/TCOMM.2003.816971.
URL http://ieeexplore.ieee.org/document/1231647/
[67] F. Benedetto, G. Giunta, L. Vandendorpe, LOS/NLOS detection by the normalized Rayleigh-ness test, in: 2009 17th European Signal Processing Conference, 2009, pp. 2131–2135.

[68] J. Antoni, J. Griffaton, H. André, L. D. Avendaño-Valencia, F. Bonnardot, O. Cardona-Morales, G. Castellanos-Dominguez, A. P. Daga, Q. Leclère, C. M. Vicuña, D. Q. Acuña, A. P. Ompusunggu, E. F. Sierra-Alonso, Feedback on the Surveillance 8 challenge: Vibration-based diagnosis of a Safran aircraft engine, Mechanical Systems and Signal Processing 97 (2017) 112–144. doi:10.1016/j.ymssp.2017.01.037.
URL https://linkinghub.elsevier.com/retrieve/pii/S0888327017300584

[69] F. Bonnardot, J. Antoni, R. Randall, M. El Badaoui, Enhancement of second-order cyclostationary signals: application to vibration analysis, in: 2004 IEEE International Conference on Acoustics, Speech, and Signal Processing, Vol. 2, IEEE, Montreal, Que., Canada, 2004, pp. ii–781–4. doi:10.1109/ICASSP.2004.1326374.
URL http://ieeexplore.ieee.org/document/1326374/

[70] P. O. Hoyer, Non-negative matrix factorization with sparseness constraints., Journal of machine learning research 5 (9) (2004).